

## Table of Contents

1. Introduction and Background .....	3
2. Computational Methods .....	8
2.1. Cluster Dynamics.....	8
2.2. Heterogeneous Nucleation.....	10
2.3. Radiation Enhanced Diffusion.....	12
2.4. Presentation of the Results .....	15
3. Atom Probe Tomography Data Used to Validate and Calibrate the CD Model .....	15
4. Results .....	17
4.1. Fe-Mn-Ni-Si System Thermodynamics at $\approx 300^{\circ}\text{C}$ .....	17
4.2. Radiation Enhanced Precipitation Kinetics.....	18
5. Calibrated CD Model Predictions of Effects of Composition and Temperature on MNSPs	
23	
5.1. The Effect of Composition .....	23
5.2. Effect of Temperature .....	24
6. Analysis of the Large CD Database on the MNSP Mole Fraction ( $f$ ) .....	25
6.1. Alloy Composition and Fluence Effects .....	25
6.2. Temperature Effects.....	26
7. Yield Stress Shift ( $\Delta\sigma_y$ ) and Ductile to Brittle Transition Temperature Shift ( $\Delta T$ ) Based on the CD-based Precipitation Model Predictions.....	26
8. Conclusions.....	27
Acknowledgements .....	29
Reference.....	30

# Thermodynamic and kinetic modeling of Mn-Ni-Si precipitates in low-Cu reactor pressure vessel

## steels<sup>1</sup>

Huibin Ke <sup>a</sup>, Peter Wells <sup>b</sup>, Philip D. Edmondson <sup>c</sup>, Nathan Almirall <sup>d</sup>, Leland Barnard <sup>e</sup>, G. Robert Odette <sup>b, d</sup>, Dane Morgan <sup>a, f, \*</sup>

<sup>a</sup> Department of Materials Science and Engineering, University of Wisconsin, Madison, WI 53706, USA

<sup>b</sup> Mechanical Engineering, University of California, Santa Barbara, CA 93106, USA

<sup>c</sup> Materials Science and Technology Division, Oak Ridge National Laboratory, Oak Ridge, TN 37831, USA

<sup>d</sup> Materials Department, University of California, Santa Barbara, CA 93106, USA

<sup>e</sup> Elysium Industries, Boston, MA 02111, USA

<sup>f</sup> Materials Science Program, University of Wisconsin, Madison, WI 53706, USA

\* Corresponding author. E-mail address: ddmorgan@wisc.edu

Abstract (*better <200 words, can't exceed 250 words*)

Formation of large volume fractions of Mn-Ni-Si precipitates (MNSPs) causes excess irradiation embrittlement of reactor pressure vessel (RPV) steels at high-extended life fluences. Thus a semi-empirical cluster dynamics model was developed to study the evolution of MNSPs in low-Cu RPV steels. The model is based on CALPHAD thermodynamics and radiation enhanced diffusion kinetics. The thermodynamics dictates the compositional and temperature dependence of the free energy reductions that drive precipitation. The model treats both homogeneous and heterogeneous nucleation, where the latter occurs on cascade damage. The model has only 4 adjustable parameters that were fit to atom probe tomography (APT) database. The model predictions are in semi-quantitative agreement with systematic Mn, Ni and Si composition variations in the alloys characterized by APT, including a sensitivity to local tip-to-tip variations even in the same steel. The model predicts that heterogeneous nucleation plays a critical role in

---

<sup>1</sup> Notice of Copyright This manuscript has been authored by UT-Battelle, LLC under Contract No. DE-AC05-00OR22725 with the U.S. Department of Energy. The United States Government retains and the publisher, by accepting the article for publication, acknowledges that the United States Government retains a non-exclusive, paid-up, irrevocable, world-wide license to publish or reproduce the published form of this manuscript, or allow others to do so, for United States Government purposes. The Department of Energy will provide public access to these results of federally sponsored research in accordance with the DOE Public Access Plan (<http://energy.gov/downloads/doe-public-access-plan>).

MNSP formation at lower alloy Ni contents, and that even small irradiation temperature variations can have a large effect on the precipitate evolution. Single variable assessments of compositional effects show that Ni plays a dominant role, while within normal ranges Mn and Si have a finite, but smaller effect. The delayed evolution of MNSPs, which have been called late blooming phases, is reasonably predicted by the model. For purposes of illustration, rather than prediction, the effect of MNSPs on transition temperature shifts are presented based on well-established microstructure-property and property-property models.

*Keywords:* Precipitation kinetics, Modeling, Mean-field analysis, Reactor pressure vessel steels, Metal and alloys, irradiation effect, ferritic steels, Microstructure, Multicomponent, Nanoparticles, Nucleation and growth, Thermodynamic modeling, Thermodynamics

## 1. Introduction and Background

Nuclear power contributes about 19.5% of the electricity supply in the United States [1], and about 13% worldwide [2]. If this major source of carbon-free energy is to be sustained, life extension of the current fleet of light water reactors will be required to bridge the gap to new plant builds [3]. Life extension will require clear demonstration of large safety margins and reliable and economic long-term plant operation. A key challenge is understanding and managing a large number of materials aging and degradation issues, ranging from concrete and cables, to reactor internals, and to pressure boundary steels [4, 5]. Thus extensive aging research is being conducted to support extending plant life from 40 (the original license) and 60 years (the first license extension), to 80 years, or more, based on a second license extension.

One critical life extension issue is neutron irradiation embrittlement of reactor pressure vessels (RPVs). RPVs are massive, thick-walled, permanent structures, whose primary function is to pressurize water from 7 (Boiling Water Reactors, BWRs) to 14 MPa (Pressurized Water

Reactors, PWRs), thereby permitting reactor operating temperatures around 290°C [6]. RPVs are also an important barrier to the release of radioactivity in the event of a core damaging accident. Regulations require very low RPV failure probabilities by crack propagation, both for normal operation and postulated accident events. In the unirradiated condition, low alloy RPV steels are very tough, and vessel fracture probabilities are negligibly small, representing no significant risk. However, neutrons leaking from the reactor core cause irradiation hardening and embrittlement, manifested as upward shifts in the ductile-to-brittle transition temperature,  $\Delta T$ , that may challenge continued safe vessel operation for some plants during extended life.

Current embrittlement regulations are based on correlations of surveillance data for a large number of RPV steels irradiated at low flux in operating reactors<sup>2</sup>. However, current  $\Delta T$  models are valid only up to about one half the peak neutron fluence that would be experienced by some vessels in the PWR fleet under extended life operation, which is about  $1 \times 10^{24} \text{ n} \cdot \text{m}^{-2}$  at 80 years (for a flux of  $\approx 5 \times 10^{14} \text{ n} \cdot \text{m}^{-2} \text{ s}^{-1}$ ). Notably, current regulatory models under-predict test reactor  $\Delta T$  for these extended-life fluences in high flux test reactor experiments [7].

It is now understood that this under prediction is due to the emergence of new hardening and embrittlement mechanisms at high fluence [7]. The most important mechanism is nucleation and growth of Mn-Ni-Si precipitates (MNSPs), as long ago predicted by Odette and co-workers [8-11]. This early work extended previous studies by Odette that demonstrated and modeled hardening and embrittlement mechanisms associated with the rapid formation of nm-scale coherent Cu precipitates that act as obstacles to dislocation glide [12]. Researchers soon recognized that the copper rich precipitates (CRPs) are highly alloyed with Mn and Ni [8, 9].

---

<sup>2</sup> RPVs are basically one-of-a-kind individually built structures, with a wide range of steel metallurgical variables (composition, start of life microstructure and product form) that are exposed to a range of irradiation variables (neutron flux, fluence, spectrum and temperature). Embrittlement is controlled by synergistic interactions between these variables acting in combination.

Mn-Ni synergisms rationalized the strong effects of the alloying element Ni, as well as impurity Cu, on hardening and embrittlement [10]. In the early 1990s Odette and coworkers carried out CALPHAD [8] based thermodynamic calculations, suggesting that Mn-Ni precipitates could form even in low Cu steels, which would otherwise be relatively insensitive to embrittlement. The Mn-Ni precipitates were predicted to be slow to nucleate and grow, thus they were dubbed late blooming phases (LBP).

These models equilibrated Mn, Ni and Cu in solution with these solutes in a specified number density of CRPs and included the effects of composition on the interface energy [8]. At sufficiently high Ni and at lower temperatures, the precipitates contain more Mn and Ni than Cu. This mean field thermodynamic modeling was later extended to include Si in Lattice Monte Carlo (LMC) simulations, based on pair-bond energy estimates extracted from CALPHAD, that predicted Cu-rich core and Mn-Ni-Si-rich shell precipitate structures [10]. Such core shell structures were also observed in atom probe tomography studies [13-16]. The early models predicted that low irradiation temperatures, high Ni and even small amounts of Cu enhance the formation of Mn-Ni and MNSPs. It was also envisioned that MNSPs heterogeneously nucleate on small Cu-Mn-Ni-Si-defect cluster complexes that form in displacement cascades. These complexes are referred to as stable matrix features (SMF). The SMF are responsible for low-to-intermediate fluence embrittlement in low Cu (< 0.07 wt.%) steels prior to the development of well-formed MNSPs which evolve from them. Since there is much more Mn + Ni + Si (typically > 2 at.%) in RPV steels than Cu (effectively less than 0.25 at%), large mole fractions ( $f$ ) of MNSPs can produce correspondingly large amounts of hardening and embrittlement, that roughly scale with  $\sqrt{f}$ .

The early models led to a systematic search for MNSPs, especially as part of the UCSB IVAR program [17]. While unrecognized glimpses of MNSPs could be found in the literature, the first results clearly showing their existence were reported by Odette in 2004 in a split-melt RPV steel containing only 0.01 wt.% Cu [18]. However, MNSPs are now widely observed in test reactor [13, 15, 16, 19, 20] and surveillance [21, 22] irradiations. It is no longer a question of if LBP MNSPs will develop, but rather to what extent they will develop as a function of flux, fluence, temperature, and alloy composition. Remarkably, however, MNSPs are not accounted for in current regulatory models [23].

Thus the motivation for this study is to develop a rigorous physical model for LBP MNSPs in low Cu RPV steels based on the underlying thermodynamics and kinetics. The model can be used to better understand the factors controlling MNSPs evolution and support prediction of alloy embrittlement under light water reactor (LWR) life-extension conditions. It is structured to include the essential physical mechanisms, while minimizing the number of fitting parameters, and is both informed by, and compared to, experiments. The model is described in detail in Sec. 2 and SI Sec. B-G, and we briefly summarize its key characteristics here.

A cluster dynamics (CD) master equation model of the evolution of the size ( $r$ ), number density ( $N$ ) and mole fraction ( $f$ ) of MNSPs as a function of fluence, flux, temperature and alloy composition has been built. The thermodynamic terms in the master equation coefficients are extracted from a CALPHAD database. The model assumes that the MNSPs have the equilibrium compositions of either G ( $\text{Ni}_{16}\text{Si}_7\text{Mn}_6$ ) or  $\Gamma_2$  ( $\text{Mn}(\text{Ni},\text{Si})_2$ ) phases. These are the two stable phases in the Mn-Ni-Si ternary projection of the Fe-Mn-Ni-Si quaternary system that are predicted by the CALPHAD database for the compositions studied in this work at around 300°C. The kinetic terms in the CD model are based on radiation-enhanced adjustments of the estimated

thermal solute diffusion coefficients, as determined by conventional reaction diffusion equations and semi-empirical flux scaling. Heterogeneous MNSP formation on the cascade cluster complexes, as noted above, is included adding to homogeneous nucleation. The results of the CD model are compared to detailed atom probe tomography (APT) data. The interface energies, heterogeneous nucleation site size and cascade cluster production efficiency factor are the main fitting parameters.

The model can be used to interpolate and extrapolate the experimental database on RPV steels, which is both sparse and not well distributed in the high dimensional space of potentially relevant variables. The CD models also provide a foundation for more realistic but complex models, e.g., including Cu and MNSPs, and simpler, but still physical, reduced order models like Avrami-based treatments of the MNSPs evolution as a function of fluence.

The paper is organized as follows. Section 2 describes the computational models and sub models. Section 3 presents the APT database. Section 4 compares the CD model predictions to the APT results. Section 5 applies the model to predict the effects of selected variations in alloy composition and irradiation temperature on the fluence dependence of the evolution of MNSPs. Section 6 analyzes the corresponding effects of composition and temperature on MNSP mole fraction at specified fluences and temperatures in terms of composition cross-plots for the entire CD database. Section 7 illustrates the effects of MNSPs on hardening and embrittlement for typical RPV steels during life-extension based on existing microstructure-property-property models. A brief summary and conclusions are presented in Section 8.

## 2. Computational Methods

### 2.1. Cluster Dynamics

Cluster dynamics (CD) can be used to describe the nucleation, growth and coarsening of precipitates from supersaturated solid solutions. The CD model used in this work is based on Slezov's general model of the kinetics of first order phase transformations [24-27], which describes the precipitate size distribution as a function of time in terms of the transition rates into ( $J_{n-1 \rightarrow n}$ ) and out of ( $J_{n \rightarrow n+1}$ ) cluster size  $n$  from and to adjoining clusters in cluster size space. Our model also adds a heterogeneous nucleation rate ( $R_{het}$ ) of clusters of size  $n_{het}$ . Figure 1 schematically illustrates the CD model. This so-called master equation for changes in the number of clusters in size class  $n$  as a function of time ( $f(n, t)$ , m<sup>-3</sup>) can be expressed as

$$\frac{\partial f(n, t)}{\partial t} = R_{het}(n, t) + J_{n-1 \rightarrow n} - J_{n \rightarrow n+1} \quad (1)$$

The parameters needed in the homogeneous nucleation model are: a) an effective radiation enhanced diffusion coefficient ( $D_{eff}$ ); b) the bulk free energy of formation of a cluster phase ( $\Delta g$ ); and, c) the cluster interfacial energy ( $\gamma$ ). Detailed expressions used in applying this model are given in SI Sec. B and a corresponding derivation is found in Chapter 2 of Ref. [27]. More details regarding the  $R_{het}$  are presented in Sec. 2.2 and SI Sec. D.

The coupled set of ordinary differential equations (ODEs) in Eq. (1) are integrated to calculate  $f_n(t)$  for  $n = 1$  to  $n_{max}$ . In the case of precipitation of a single solute species with monomer transitions, as is assumed here, the integrations are trivial, even for a large  $n_{max}$ . However, in this case the clusters are composed of three species, in this case specifically Mn, Ni and Si. Thus, in principle, it would be necessary to solve clustering ODE for these three solute dimensions, potentially involving integrating up to  $O(n_{max}^3)$  equations (see SI Sec. B for derivation), which would be computationally prohibitive. To avoid this complication, it is

assumed that the clusters grow and shrink by absorbing or emitting pseudo monomers molecules that are composed of Mn, Ni and Si with the stoichiometric composition of the precipitating phase.

The cluster pseudo solute emission rates are based on a detailed balance between adjoining cluster sizes, which depends on the cluster free energies of formation and the radiation enhanced diffusion kinetics. The formation free energy of clusters with  $n$  atoms for a dilute solution model can be written in terms of a solute product as

$$\Delta G(n) = n\Delta g + \sigma(n) = nk_B T \ln\left(\frac{\bar{K}_{sp}}{K_{sp}}\right) + 4\pi r_n^2 \gamma \quad (2)$$

where  $\Delta g$  is the formation free energy per atom of an infinite bulk precipitate phase,  $\sigma(n)$  is the interfacial energy for clusters with  $n$  atoms with radius  $r_n$  and an interfacial energy per unit area of  $\gamma$ ,  $k_B$  is the Boltzman constant,  $T$  is temperature. The solute product,  $K_{sp}$ , is defined as

$$K_{sp} = \prod_i c_i^{x_i} \quad (3)$$

Here  $c_i$  is the instantaneous composition of each dissolved element in the alloy matrix and  $x_i$  is the composition of the element in the precipitate phase. The solute product at equilibrium is denoted as  $\bar{K}_{sp}$ . The classical derivation and justification of the relation between solute products and formation energy of precipitates is provided in SI Sec. B. Solute products are determined from CALPHAD thermodynamic models, as described in Sec. 4.2. Interfacial energies were fit to experimental data, again as described in Sec. 4.2. The radiation enhanced diffusion kinetics was determined from literature measurements of thermal diffusion, previously parameterized models for point defect generation and evolution at low flux, and a previously derived simple *effective* flux scaling model [28]. Details are provided in Sec. 2.3 and SI Sec. B and C.

It is useful to draw a simple picture of what the CD model treats. Initially precipitation is dominated by clustering and precipitate nucleation and the initial stages of growth. However,

nucleation rates decrease rapidly as the solutes are depleted supersaturated matrix. This gives rise to an overlapping region dominated by precipitate growth. However, growth rates also decrease with dissolved solute depletion, and becomes negligible as the Gibbs-Thomson effect modified solubility limit is approached. This condition gives rise to a third overlapping region dominated by precipitate coarsening. Notably, the CD model treats all of these processes seamlessly, and in a way that directly connects to the underlying thermodynamics and kinetics.

## 2.2. Heterogeneous Nucleation

Heterogeneous nucleation is a critical element of the model. Here we assume that clusters of size  $n$  are generated in displacement cascades at a rate  $R_{het}(n,t)$ , which has units of number of clusters generated per unit volume and per unit time. The underlying mechanism is that the high concentrations of point defects in the cascades, during both formation and much longer time aging periods, lead to defect-solute cluster complex formation due to corresponding defect-solute binding energies. The first model for defect solute complex formation (Cu-coated nanovoids) was first proposed by Odette [9] and later confirmed by a number of Kinetic Lattice Monte Carlo models of cascade aging [11, 29]. Further discussion of the rich physics of cascade aging in alloys is beyond the scope of this paper, but it is sufficient to note that rather large solute cluster complexes, and their solute remnants, form in cascades at some frequency that decreases with their size.

$R_{het}$  is proportional to the cascade production rate per atom,  $\sigma_{cas}\phi/\Omega$ , where  $\sigma_{cas}$  is the cascade production cross section,  $\phi$  is the neutron flux, and  $\Omega$  is the atomic volume.  $R_{het}$  also depends on the amount of the remaining dissolved solute, which we represent by the ratio of the instantaneous triple product  $K_{sp}$  to a reference  $K_{sp}^0$ . Finally, the fact that at a given  $K_{sp}$  only a fraction of cascades produce a large cluster of defined size  $n$ , is represented by a cascade cluster

production efficiency factor,  $\alpha$ , at  $K_{sp}$ . While there is a distribution of  $n$  that can contribute to heterogeneous nucleation, for simplicity assume that only clusters of size  $n_{het}$  are generated. Thus  $R_{het}$  is given by

$$R_{het}(n_{het}, t) = \alpha \cdot \frac{\sigma_{cas}\phi}{\Omega} \cdot \frac{K_{sp}(t)}{K_{sp}^0}, \quad (4)$$

and  $R_{het}(n \neq n_{het}, t) = 0$ .

The efficiency factor,  $\alpha$ , is a fitting parameter representing the fraction of cascades that produce a cluster of size  $n_{het}$  when the solute product is at equilibrium ( $K_{sp}(t) = K_{sp}^0$ ). The physical basis for  $\alpha$  is partly stochastic, and partly associated with the energy of the primary knock-on atom (PKA) that creates the cascade (note, PKAs are generated by fast neutrons over a wide range of recoil energies). However, given the complexity of forming defect solute complexes in displacement cascades,  $\alpha$  is treated as the second heterogeneous fitting parameter.

While rooted in plausible physics, this nucleation model is a surrogate for more complex mechanisms of heterogeneous nucleation that may include solute segregation to ex-cascade small loops and nanovoids. Note, this treatment does not include the role of dislocations and grain boundaries in heterogeneous nucleation, although both are observed experimentally, especially for conditions of low solute supersaturations. Further, the present model does not treat the potential role of Cu. While the alloys studied here have low Cu contents, it has long been observed and predicted that small amounts of this element, even below the concentration for well-formed precipitates, can enhance MNSP nucleation [8]. Such effects, to the extent they are significant, are effectively renormalized into the fitting parameters in the model. These approximations will be dealt with in future work and are discussed further in SI Sec. D.

### 2.3. Radiation Enhanced Diffusion

The cluster dynamics model used in this work requires Mn, Ni, and Si diffusion coefficients under irradiation. The diffusion of these species is accelerated by excess vacancies produced under irradiation, a phenomenon generally referred to as radiation enhanced diffusion (RED). A model for RED is used in this work that accounts for flux effects with a simple power law-scaling model. We use a simplified version of a RED model developed by Odette et al. that accounts for solute vacancy trap enhanced recombination and extra annihilation of vacancies and self-interstitial atoms at transient sinks formed in cascades [28, 30, 31].

Here the thermal diffusion coefficients  $D^{th}$  are given by the standard expression

$$D^{th} = D_0^{th} \exp\left(-\frac{Q}{kT}\right) \quad (5)$$

Unfortunately, there is essentially no diffusion data for Mn, Ni, and Si in Fe at the relevant LWR temperatures of about 300°C. Thus estimating the  $D^{th}$  requires a large extrapolation from high temperature. Furthermore, the low temperature  $D^{th}$  must account for the effects of changing ferromagnetic state on the migration energetics of the solute below the Curie temperature. Although self-diffusion coefficients of Fe have been studied by a number of researchers, for example [32-38], there is very limited experimental data on the thermal diffusion coefficients of Mn, Ni, and Si solutes in ferromagnetic Fe. Indeed, to our knowledge, there is only one dataset for Mn [39] and one for Ni [40], and none for Si.

Therefore, we have developed an approximate, but internally consistent, approach to estimate together the diffusion coefficient for Fe and all the impurities based on constant activation energy models fit to data for the ferromagnetic host Fe. Details about how the thermal diffusion coefficients were obtained are given in SI Sec. F. In the CD model the thermal diffusion coefficients for the individual solutes were then adjusted to give the RED coefficients

(as described below) and then further combined into one effective value based on the composition of the matrix and precipitates, as described in SI Sec. C and Ref. [30].

The RED coefficient,  $D^*$ , can most simply be expressed as [30]

$$D^* = D_v X_v \frac{D^{th}}{D^{sd}} + D^{th} \quad (6)$$

$D^*$  is the diffusion coefficient for a given species used in the cluster dynamics model (see SI Sec. B),  $D^{th}$  is the thermal diffusion coefficient of solute,  $D^{sd}$  is the self-diffusion coefficient of the solvent Fe,  $D_v$  is the diffusion coefficient of vacancies and  $X_v$  is vacancy concentration under irradiation. At steady state, when defect production and annihilation rates balance,  $X_v$  is given by [30]

$$X_v = \frac{g_s \xi \sigma_{dpa} \phi}{Z_t D_v} \quad (7)$$

Here,  $\xi$  is the cascade surviving defect production to dpa efficiency factor,  $\sigma_{dpa}$  is the dpa cross-section,  $Z_t$  is the total sink strength,  $D_v$  is the vacancy diffusion coefficient and  $g_s(\phi, T, Z_t, \dots)$  is the fraction of migrating defects that escape recombination to reach sinks [30]. The detailed model for  $g_s$  accounts for flux dependent solute trap recombination, with  $g_s < 1$ . The expression for  $g_s(\phi, T, Z_t, \dots)$  is complex and contains a number of parameters, like vacancy trapping energy and solute trap concentrations. Thus we have chosen a simpler expedient and express  $D^*$  as a function of flux as [30]

$$D^* = D^{th} \frac{\xi \sigma_{dpa} [g_s(\phi_r) (\phi_r/\phi)^p]}{Z_t D^{sd}} \phi = k(\phi, \dots) \phi \quad (8)$$

Here  $\phi_r$  is an arbitrarily selected reference flux. Within the brackets, the first term represents the sink dominated case when  $g_s(\phi_r) \approx 1$ , while the second term  $(\phi_r/\phi)^p$  accounts for increasing recombination with increasing flux.

The effective time evolution of the model is set by both the diffusion rates and the heterogeneous nucleation rate. Ignoring the latter for the moment, the scaling in Eq. (7) means

that the time evolution of the system is controlled by an effective time  $t_e = t(\phi_r/\phi)^p$ . This time scaling allows us to define an effective fluence,

$$\phi t_e = \phi t(\phi_r/\phi)^p \quad (9)$$

where  $\phi t$  is the actual fluence. The effective fluence accounts for how flux affects the excess irradiation induced vacancies that accelerate diffusion. In the  $g_s = 1$  sink-dominated limit there is no flux effect on  $D^* t$ , while in the recombination dominated limit  $g_s$  is proportional to  $(\phi_r/\phi)^{0.5}$ . Thus higher flux delays MNSP (and CRP) evolution. Independent analysis has shown  $p$  typically varies between  $\approx 0.15$  and  $0.35$  over a wide range of higher flux (or equivalent dpa rates for charged particle irradiations) [31]. Thus a nominal value of  $p = 0.2$  was used in this work. We also selected a reference flux  $\phi_r = 3 \times 10^{15} \text{ n} \cdot \text{m}^{-2} \text{s}^{-1}$  [30]. Note, the low flux is consistent with being in a nearly sink dominated regime with  $g_s \approx 1$  [30].

However, we note that in our model the heterogeneous nucleation term,  $R_{het}$ , depends directly on flux (as described in Sec. 2.2), therefore has a time dependence that scales with  $t$  rather than with  $t_e$ . However, the CD model directly accounts for this effect on heterogeneous nucleation. We also note that the  $k(\phi)$  in Eq. (7) is almost certain to vary somewhat from alloy to alloy, and for different irradiation conditions, in a way that is not fully modeled by the multi element  $D^h$  and  $p$ -flux scaling approach. Thus the predictions of the precipitate size distribution,  $r$ ,  $N$  and  $f$  would be expected to move to higher or lower positions on the fluence axis depending on the individual case. While it could be argued that each particular set of alloy-irradiation conditions (say CM6 and ATR-1 – see below) should be individually fit for  $D^*$ , we chose to use only one calculated  $D^*(\phi_r)$  along with the  $p$ -scaling flux adjustment, so that the model can be applied across many alloys and used to model new situations where fitting  $D^*$  is not possible. In

spite of its approximate nature and simplicity, as shown below, the unfitted treatment of  $D^*$  works remarkably well within the context of the current objectives of the model.

#### 2.4. Presentation of the Results

The CD model predicts the precipitate number density  $N$ , size distribution  $N(r)$ , mean radius  $\bar{r}$ , and mole fraction  $f$  (see SI Sec. E for definitions of how each of these are determined), as a function of fluence. The CD calculations were carried out as a function of alloy composition and temperature. As discussed below in Sec. 3, the models used the actual local chemistries of various atom probe tips and the estimated temperature of the irradiation when comparisons are made with experimental data. In all cases, when determining quantities from the CD calculations we exclude all cluster sizes below 65 atoms. The minimum number of precipitate atoms in APT experiments is 15-30 [16]. This value is based on a detection efficiency of about 37% and the fact that the APT measurements do not detect solute clusters smaller than about 40-80 atoms.

### 3. Atom Probe Tomography Data Used to Validate and Calibrate the CD Model

Five RPV steels irradiated in four reactors were studied. The irradiations included the high flux test reactors, Advanced Test Reactor (ATR) and Belgian Reactor 2 (BR2), and low flux reactor surveillance capsules in the Ringhals and Ginna power plants. Flux and fluence varied from  $5.9 \times 10^{14} \text{n} \cdot \text{m}^{-2} \text{s}^{-1}$  to  $2.3 \times 10^{18} \text{n} \cdot \text{m}^{-2} \text{s}^{-1}$  and  $3.3 \times 10^{23} \text{n} \cdot \text{m}^{-2}$  to  $1.1 \times 10^{25} \text{n} \cdot \text{m}^{-2}$  (or dose from 0.0495 to 1.65dpa [30]), respectively. The nominal temperature ranged from 284°C to 300°C. However, a recent as-run reevaluation placed the ATR-1 temperature at  $\approx 320^\circ\text{C}$ , so this adjusted value was used in this work. The test reactor irradiations included Cu free plate (LG) and forging (CM6) that contain  $\approx 0.75$  to 0.85 wt% Ni and 1.35 to 1.65 wt.% Ni, respectively. These steels have bainitic microstructures and properties characteristic of in-service steels. The steels in the

surveillance irradiations were all low Cu (< 0.07 wt.%) steels with intermediate (Ginna) and high (Ringhals) Ni contents, respectively. The data sets are identified by the irradiation condition and alloy designation. However, since the main variables are the Ni content and flux and fluence, in addition to the identification cited above, a parenthetical notation is added to designate a low (L), medium (M) or high (H) category, for these compositional and irradiation variables, respectively. The parenthesis gives a 3-tuple whose order corresponds to Ni content, flux, and fluence. For example, Ringhals N is categorized as (HLM), meaning high Ni, low flux and medium fluence, while ATR-1 LG as (MHH), meaning medium Ni and high flux and high fluence. Note that these designations do not account for variations in alloy Mn and Si contents.

It was previously shown that nano-scale MNSPs respond to local alloy compositions of individual APT tips [16]. The database used in this study included up to nine APT tips per alloy, yielding a total of 33 different compositions. The average APT measured compositions and irradiation conditions are shown in Table 1. The local compositions, when more than one tip was measured, are reported in supplementary information Table SI-1.

The APT analysis method used for all the data obtained by UCSB is described in detail in reference [41]. Previously published APT on Ringhals welds [21] and Ginna forging [22] were reanalyzed by Edmondson in a way that is consistent with [41] to provide a maximal consistent data set.

Table 1 The alloy compositions and irradiation conditions in this study.

Name (Ni, flux, fluence)	Composition (at.%)			Irradiation Condition			Reference
	Mn	Ni	Si	Temperature (°C)	Flux ( $\times 10^{16}$ n·m $^{-2}$ s $^{-1}$ )	Fluence ( $\times 10^{23}$ n·m $^{-2}$ )	
Ringhals E (HLM)	1.25	1.50	0.41	284	0.147 to 0.166	6.39	[21], this work
Ringhals N (HLM)	1.14	1.68	0.28			3.3, 6.03	
Ginna Forging (MLM)	0.57	0.92	0.67	290	0.0592	5.80	[22], this work
BR2-TU LG (MMH)	1.18	0.73	0.44	300	30	25	This work
BR2-TU CM6 (HMH)	1.16	1.63	0.35				

BR2-G2 CM6 (HHM)	0.94	1.61	0.35	300	100	6.67	This work
BR2-G1 LG (MHH)	1.09	0.86	0.49			13.3	[16]
BR2-G1 CM6 (HHH)	1.09	1.34	0.33	320	230	110	
ATR-1 LG (MHH)	0.87	0.71	0.43				
ATR-1 CM6 (HHH)	1.42	1.69	0.39				

## 4. Results

### 4.1. Fe-Mn-Ni-Si System Thermodynamics at $\approx 300^\circ\text{C}$

The Thermo-Calc [42] Aluminum 2 (TCAL2) CALPHAD database [43] was used to establish the Fe-Mn-Ni-Si phase diagram as the thermodynamic foundation for this study. This thermodynamic analysis updates previous work of Xiong et al. [44]. It has been recently determined that the ATR-1 data shown in [44] was actually run at  $320^\circ$  rather than  $290^\circ\text{C}$  which was previously believed based on thermal models due to higher than initially assumed heating rates. Thus an update of the thermodynamic calculation results using a temperature of  $320^\circ\text{C}$ , as well as an explicit discussion of the Gibbs-Thomson effect on the mole fraction of the MNSPs is given in SI Sec. H.

The TCAL2 database predicts that there are two intermetallic phases at equilibrium at around  $300^\circ\text{C}$ : the T3 or G-phase,  $(\text{Mn}_6\text{Ni}_{16}\text{Si}_7)$ ; and the T6 or  $\Gamma_2$  phase,  $(\text{Mn}(\text{Ni},\text{Si})_2)$ . Their respective crystal structures are shown in Table 2 [45, 46]. Figure 2a shows that the predicted precipitate compositions compared to experimental results, for the average APT tip compositions and irradiation temperatures in this study, are in good general agreement (with RMS of 5.17%, 7.54% and 6.13% for Ni, Mn and Si, respectively). The corresponding predicted equilibrium mole fractions ( $f$ ) of each element in the MNSPs are shown in Figure 2b. No comparison is made with experiment in this case, since the nm-scale MNSPs are not in equilibrium even at the highest fluence due to a significant Gibbs-Thomson effect (comparisons are made in SI. Sec. H

for the ATR-1 condition). Figure 2c shows the predicted MNSPs and their mole fractions for each alloy. In 5 out of the 10 cases the precipitates are the stoichiometric T6/ $\Gamma_2$  phase. The T6 phase is generally associated with high Ni alloys ( $>1.6$  wt. %); however, one high Ni alloy had a very small amount of T3/G phase. One of the intermediate Ni alloys contains stoichiometric T3 phase, while two others contain both T3 and T6 phases; one has about 62% T3 and 38% T6, and the other has about 12% T3 and 88% T6. The mole fractions of these phases decrease with increasing temperature. For a nominal alloy composition of 1.0 Mn-0.6Si-0.75Ni at.%, the T3 phase persists up to 408°C, while T6 phase persists up to 430°C. When Ni is increased to 1.6 at% the T3 phase persists up to 455°C and T6 phase persists up to 487°C. Details aside, the major conclusion is that equilibrium MNSP intermetallic phases can readily form in the  $\approx 270$  to 300°C operating temperature regime of RPVs. This result is in contradiction with a number of first-principles and kinetic Monte Carlo studies arguing that MNSPs must be irradiation induced [47-49].

Table 2 The crystal structures of Mn-Ni-Si phases in RPV steels at around 300°C.

Phase	Composition	Space group	Type	Lattice constant, nm	Number of atoms in a unit cell
T3/G-phase	$Mn_6Ni_{16}Si_7$	$Fm\bar{3}m$	$Mg_6Cu_{16}Si_7$	1.108	116
T6	$Mn(Ni, Si)_2$	$Fd\bar{3}m$	$Cu_2Mg$	0.668	24

#### 4.2. Radiation Enhanced Precipitation Kinetics

The CD model was used to predict the evolution of MNSPs as a function of fluence, temperature, flux and alloy composition. The thermodynamic, thermal diffusion and other parameters used in the model are summarized in Tables 3, 4 and 5, respectively. The equilibrium solute products of the two phases at different temperatures corresponding to the nominal experimental conditions were obtained from the TCAL2 database [43] (as described in Sec. 4.1), and are listed in Table 3. Table 3 also shows the solute product at 320°C which is a newly

adjusted as-run temperature for the ATR-1 data. This temperature adjustment only affects the ATR-1 data and the consequences of this recent adjustment to the corresponding predictions are discussed below. Table 4 lists the thermal diffusion coefficient ( $D^{th}$ ) parameters as discussed in Sec. 2.3 and further in the SI Sec. F.

Table 3 The equilibrium solute product for the G-phase (T3) and  $\Gamma_2$ -phase (T6) at different temperatures.

Temperature (°C)	Equilibrium solute product ( $\times 10^{-3}$ )	
	T3	T6
280	1.96	2.33
284	2.12	2.53
290	2.21	2.56
300	2.45	2.82
320	3.02	3.42

Table 4 The thermal diffusion coefficients used in this study.

Element	$D_0$ ( $\times 10^{-4}$ m $^2$ ·s $^{-1}$ )	Q (kJ·mol $^{-1}$ )	Reference
Mn	1.49	234.0	[39]
Ni	1.4	245.6	[40]
Si	0.78	231.5	[50]
Fe	27.5	254.0	[32]

All other model parameters used in the model are listed in Table 5. Most of them were obtained from two papers [30, 51]. Four of them, highlighted in italics and denote with FIT in parentheses, are fitting parameters, including the heterogeneous nucleation size and cascade cluster production efficiency factor (see Sec. 2.2) and two interfacial energies. Please note ATR-1 data were not used to obtain the fitting parameters, due to their irradiation condition with high flux, fluence, and irradiation temperature, although comparisons between CD results and experimental data are still given. The fitting process is discussed in detail in SI Sec. G. Note that the numerical fit values are all physically reasonable. In particular, the nucleation size  $n_{het}$  is relatively small, consistent with it being formed during cascade aging. Similarly,  $\alpha$  is also quite

reasonable, consistent with just a small fraction of cascades ( $\sim 1\%$ ) producing heterogeneous nucleation sites at low supersaturations. Both the T3 and T6 interfacial energies are quite similar, consistent with their similar compositions. Furthermore, both are significantly lower than the Cu-Fe interfacial energy (typically taken to be about  $0.4 \text{ J}\cdot\text{m}^{-2}$  [8]), which is consistent with the phenomena observed in experiments that Mn, Ni and Si are usually segregated to and outside the CRPs interface [13-16].

Table 5 The model parameters used in calculating the radiation enhanced diffusion coefficient and other parameters used in cluster dynamics model.

SIA – vacancy recombination radius ( $r_v$ , nm)	0.57 [30]
Fraction of vacancies and SIA created per dpa ( $\xi$ )	0.4 [30]
Displacement-per-atom (dpa) cross-section ( $\sigma_{dpa}$ , $\text{m}^2$ )	$1.5 \times 10^{-25}$ [30]
Atomic volume ( $\Omega_a$ , $\text{m}^3$ )	$1.18 \times 10^{-29}$
Vacancy diffusion coefficient pre-exponential factor ( $D_v$ , $\text{m}^2\cdot\text{s}^{-1}$ )	$1 \times 10^{-4}$ [51]
Vacancy migration energy ( $E_v^m$ , eV)	1.3 [51]
Dislocation sink strength (dislocation density) ( $\rho$ , $\text{m}^{-2}$ )	$2 \times 10^{14}$ [30]
Flux effect scaling exponential factor ( $p$ )	0.2 [31, 52]
Cascade cross section ( $\sigma_{cas}$ , $\text{m}^2$ )	$2 \times 10^{-28}$ [52]
Reference solute product ( $K_{sp}^0$ )	$2.4 \times 10^{-3}$
Heterogeneous nucleation size ( $n_{het}$ ) (FIT)	60
Cascade cluster production efficiency factor ( $\alpha$ ) (FIT)	$7.2 \times 10^{-3}$
Interfacial energy of T3 phase ( $\gamma_{T3}$ , $\text{J}\cdot\text{m}^{-2}$ ) (FIT)	0.190
Interfacial energy of T6 phase ( $\gamma_{T6}$ , $\text{J}\cdot\text{m}^{-2}$ ) (FIT)	0.175

Figure 3 and Figure 4 show the evolution of MNSPs ( $N$ ,  $\bar{r}$  and  $f$ ) as a function of fluence for all the alloys. The bands represent a range of individual tip compositions. Note CD predicts that the number density and mole fraction of the lower Ni, higher temperature ATR-1 LG (MHH coding) MNSPs are so low that they are not visible on scales used in Figure 3. The corresponding evolutions of MNSPs for the average APT tip compositions are shown in Figure SI-4. Comparisons of the CD model precipitate size distributions between and the experimental data for selective alloys are shown in Figure SI-5. The CD model predicts all the alloys are in the nucleation and growth (N&G) stages of precipitation except in the case of the high Ni ATR-1

CM6 (HHH) condition, where the early precipitation and very high fluence of  $1.1 \times 10^{25} \text{m}^{-2}$  extends into the coarsening regime. Note in the N&G regime the model-experiment comparisons are very sensitive to the accuracy of the simplified RED treatment of  $D^*$ , as discussed in Sec. 2.3.

Figure 5 shows the strong effect of higher flux in delaying precipitation by the comparing CD model predictions for nearly identical alloys (Ringhals N and CM6), both with high Ni  $\approx 1.6 \text{at. \%}$ , irradiated at widely different fluxes ( $1.49 \times 10^{15} \text{m}^{-2}\text{s}^{-1}$  for Ringhals up to  $2.3 \times 10^{18} \text{m}^{-2}\text{s}^{-1}$  for ATR-1). The simple  $p = 0.2$  scaling leads to a factor of 4.34 increase in the fluence required to generate similar fractions of precipitation for the ATR-1 flux which is 1544 times higher than the Ringhals surveillance flux condition. The experimental data for CM6 at the lower fluences are also for high fluxes, but ones that are somewhat less than in ATR-1 (TU, G1, G2 see Table 1). Thus they are plotted at an effective higher fluence using the same  $p$ -scaling adjustment to the reference ATR-1 flux, as indicated by the arrows. Notably, the observed effect of flux effects is larger than predicted by the  $p$ -scaling model. It is useful to be reminded that the fluence indexing of the two curves is governed by  $D^*/f$  and that besides being oversimplified the use of the canonical average  $p = 0.2$  increases the approximate nature of the  $D^*$  model. For example, it is known that the higher Ni contents in CM6 and Ringhals lead to a higher rate of solute vacancy trap recombination, which corresponds to a larger effective  $p$  [30]. More generally the agreement between the CD model predictions and experiment would be enhanced if  $D^*$  itself were treated as a fitting parameter for individual alloys.

Figure 6 provides a more detailed one-on-one comparison of the predicted cluster dynamics precipitate  $\bar{r}$ ,  $N$  and  $f$  with APT measurements. If we exclude the ATR-1 experiments, the agreement is reasonable across this large range of compositions and irradiation conditions.

However, the mole fractions of the MNSPs during the growth stage for the medium Ni alloys (BR2-TU MMH LG, BR2-G1 MHH LG and MLM Ginna) are all under-predicted by the model. These differences are most likely caused either by uncertainties in the thermodynamic parameterization and RED model or unmodeled physics, where the later may include dislocation and, especially, small loop enhanced nucleation and solute segregation, including that driven by radiation induced segregation (RIS). The predicted and measured values for LG (LHH) and CM6 (HHH) under the ATR-1 irradiation conditions (using the recently updated temperature of 320°C) are shown as the open symbols. These results were not included in the parameter fitting, since the very high flux, fluence and high temperature irradiation condition is well beyond the corresponding range for LWR service and more relevant test reactor data. However, it's still useful to show the comparisons between the CD model predictions and the experimental data for this extreme condition. MNSPs are significantly under-predicted by the CD model in this case, particularly for LG. Actually, the experimentally observed mole fractions of MNSPs for these alloys are even higher than what were predicted by CALPHAD model at equilibrium without considering the Gibbs-Thomson effect (see SI Sec. H). Therefore, unmodeled physics might be playing a significant role, including that is due to the very high flux used in the ATR-1 experiment. For example, this could be related to the influence of small amounts of Cu, or segregation at small, surviving, ex-cascade dislocation loops. In general, dislocation assisted nucleation is expected, especially for cases like LG with lower Ni concentration and free energy differences driving precipitation [22]. Note, after the MNSPs have grown, their small loops nucleation sites would be consumed, or not apparent, making their role difficult to identify.

Overall, except for the confounded ATR-1 data, the CD model predictions are in semi-quantitative agreement with experimental APT measurements of MNSP  $N$ ,  $\bar{r}$  and  $f$ , as well as the

observed MNSP size distribution. Given the complexity of multicomponent precipitation under irradiation and the wide range of compositions and irradiation conditions considered, this level of agreement suggests that the model reasonably represents the dominant underlying physics of MNSPs evolution under irradiation. Most importantly, the model can be used to better understand the role of different mechanisms, and assess the influence of key material and irradiation variables for low Cu steels under both test reactor and vessel service LWR irradiation conditions.

As an example of possible mechanistic insight, Figure 7 shows the ratio of number density of MNSPs formed by heterogeneous nucleation to homogeneous nucleation at fluences of 1, 5 and  $10 \times 10^{23} \text{ n}\cdot\text{m}^{-2}$ . In all cases heterogeneous nucleation is dominant at lower fluence and in 6 out of 8 cases it is dominant even at high fluence. Plots of number density of MNSPs of different phases formed by different nucleation mechanisms as a function of fluence are shown in the supplemental information Figure SI-6.

In summary, the success of the present model strongly suggests that vacancy enhanced diffusion dominates MNSP growth and that radiation induced effects associated with cascades can play a major role in their nucleation for medium Ni steels with relatively lower driving forces for homogeneous nucleation. Furthermore, the discrepancies in the model predictions suggest that segregation at small surviving ex-cascade dislocation loops, which are not modeled may play an important role in nucleation, especially in low solute steels, at high flux and fluence.

## 5. Calibrated CD Model Predictions of Effects of Composition and Temperature on MNSPs

### 5.1. The Effect of Composition

Atom probe tomography (APT) is a powerful tool for three-dimensional nano-analytical mapping with near atomic-scale resolution [53]. However, the volume of the analyzed region is typically  $\approx 2$  to  $4 \times 10^4$  nm<sup>3</sup>, corresponding to  $\approx 5$  to  $40 \times 10^6$  atoms and length scales of 25 to 35 nm. Such tiny volumes are subject to significant tip-to-tip composition fluctuations in typical micro-segregated steels. For example, if a particular tip contains, or is adjacent to, a large carbide, it is likely to contain significantly less than the average Mn content, which is always lower than the bulk content in any event. Both Si and Ni are controlled by the specific alloy solute additions, but these also vary somewhat from tip to tip. Thus as has been shown [16] the precipitation in a tip is strongly affected by the local solute concentration. Indeed tip-to-tip chemistry variations can be exploited to establish dissolved solute-precipitate relationships [16]. In this work we used the actual matrix Mn, Ni and Si compositions measured by APT in modeling MNSPs evolutions. Figure 8 highlights the compositional sensitivity for irradiations at a flux of  $10^{16}$  n·m<sup>-2</sup>s<sup>-1</sup> at 290°C. Figure 7a shows the effects of intermediate Ni (0.80, 1.10at%) and lower Mn contents (0.80, 1.10at%), while Figure 7b is for high Ni (1.45, 1.75at%) and slightly higher Mn (1.00, 1.30at%). These values are in the range of the in service type RPV alloys studied here. As expected, the MNSP  $N$  and  $f$  systematically increase with Mn and Ni. The corresponding  $\bar{r}$  values are somewhat less sensitive to composition variations, especially at higher Ni. Composition also systematically affects both the pre- and post-saturation regimes of MNSP  $N$  and  $f$ . Clearly, higher Ni has a powerful effect on lowering the fluence associated with the rapid MNSP formation with high  $N$  and  $f$ . Further, in both cases, there are only slightly overlapping

regions of nucleation and growth, since  $N$  is nearly saturated (or decreasing slightly) when  $f$  begins to rapidly increase. This observation rationalizes some of the confusion regarding the character of MNSPs. That is, a high number density of sub nm MNSPs form before they begin to grow rapidly, and are not easily identified as well-formed precipitates. Note the dominant nucleation mechanism also varies between the medium (heterogeneous) and high Ni (homogeneous) regimes. The different effects of alloy composition are discussed further in Sec. 6 below and the corresponding effects of the computed  $f$  on hardening and the resulting  $\Delta T$  for different for low flux reactor conditions is presented in Sec. 7 and SI Sec. I.

## 5.2. Effect of Temperature

MNSPs evolution is also very sensitive to the irradiation temperature, which is significant for a number of reasons. First the temperatures in this study varied over a nominal range of  $\approx 290$  to  $300^{\circ}\text{C}$ , and in practice up to  $\approx 320^{\circ}\text{C}$  in the actual as-run condition for ATR-1. Typical in service power reactor vessel temperatures range from  $\approx 270^{\circ}\text{C}$  to  $300^{\circ}\text{C}$ . Further, it is extremely difficult to accurately control and measure temperatures to uncertainties less  $\approx \pm 10\text{--}15^{\circ}\text{C}$ . Notably, the effects of temperature are also very sensitive to the alloy composition.

Figure 9 shows the effect of temperature on the evolution of MNSPs, modeled for two compositions: a high solute 1.45at.%Mn-1.65%Ni-0.45%Si and a low solute 1.00at.%Mn-0.70%Ni-0.35%Si composition, respectively. The results are shown for a flux  $10^{16}\text{n}\cdot\text{m}^{-2}\text{s}^{-1}$  up to  $10^{25}\text{n}\cdot\text{m}^{-2}$  at 280, 290 and  $300^{\circ}\text{C}$ . The effect of these variations of temperature mainly occurs during the nucleation stage of precipitation associated with the rapid increase in  $N$ , which can differ up to five times for high solute alloy and up to 10 times for low solute alloy for only a  $20^{\circ}\text{C}$  temperature difference. The effect of temperature on  $N$  is also reflected mole fraction of MNSPs that can differ up to 1.0% for high solute alloys and 0.7% for low solute alloys. There is

only a minor corresponding effect on the mean MNSP radius,  $\bar{r}$ . These results demonstrate that temperature effects must be carefully considered when comparing experimental with the CD model predictions.

## 6. Analysis of the Large CD Database on the MNSP Mole Fraction ( $f$ )

### 6.1. Alloy Composition and Fluence Effects

In this section, we model the combined effect on MNSPs mole fraction of a range of RPV alloy compositions, irradiation temperatures ( $T$ ) and fluences ( $\phi t$ ) presented as a series of cross plots of  $\sqrt{f}$  versus a single variable, while holding the other variables constant. As discussed below, irradiation hardening ( $\Delta\sigma_y$ ) and embrittlement ( $\Delta T$ ) primarily depend of the  $\sqrt{f}$ . Figure 10 shows cross plots of the  $\sqrt{f}$  versus Ni, over the specified range of Mn and Si at  $10^{23}$ ,  $5 \times 10^{23}$  and  $10^{24} \text{ n} \cdot \text{m}^{-2}$  at  $290^\circ\text{C}$  and a flux of  $3 \times 10^{15} \text{ n} \cdot \text{m}^{-2} \text{ s}^{-1}$ . As discussed below, the  $\sqrt{f}$  is used since it's the primary MNSP characteristic that controls  $\Delta\sigma_y$  and  $\Delta T$ .

Clearly Ni has a dominant effect on  $\sqrt{f}$ . The effects of Mn and Si are significant but more modest than they are for Ni. The absolute MNSP  $\sqrt{f}$  is low at  $10^{23} \text{ n} \cdot \text{m}^{-2}$ , but increases somewhat starting at  $\approx 1.5 \text{ at.\%Ni}$ . The effect of Ni is much stronger at  $5 \times 10^{23} \text{ n} \cdot \text{m}^{-2}$  above  $\approx 0.5 \text{ at.\%Ni}$ , and  $\sqrt{f}$  again increases rapidly above  $\approx 1.5 \text{ at.\%Ni}$ . At  $10^{24} \text{ n} \cdot \text{m}^{-2}$   $\sqrt{f}$  increases approximately linearly, or with a weak polynomial dependence, between  $0.5 \text{ at.\%}$  and  $1.6 \text{ at.\%Ni}$ , and at higher Ni the increase in  $\sqrt{f}$  begins to taper off. SI Sec. J provides a simple polynomial fit for  $\sqrt{f}$  as a function of alloy composition at  $10^{24} \text{ n} \cdot \text{m}^{-2}$  and  $290^\circ\text{C}$ .

### 6.2. Temperature Effects

The MNSP  $f$  also depends strongly on the irradiation temperature ( $T$ ). Figure 11 plots  $\sqrt{f}$  versus  $T$  at  $\text{Ni} = 0.6 \text{ at.\%}$ ,  $1.0 \text{ at.\%}$ ,  $1.4 \text{ at.\%}$  for  $0.6 \text{ at.\%Si}$  and  $1.0 \text{ at.\%Mn}$  at fluences of  $5 \times 10^{23}$  and  $10 \times 10^{23} \text{ n} \cdot \text{m}^{-2}$ . Figure 11 a) shows that the absolute  $\sqrt{f}$  increases with increasing Ni and

decreasing  $T$ . Figure 11 b) shows the same data normalized to 1 at 290°C. In all cases the  $\sqrt{f}$  versus  $T$  follow an approximately linear relation, and overall the trends are qualitatively similar.

## 7. Yield Stress Shift ( $\Delta\sigma_y$ ) and Ductile to Brittle Transition Temperature

### Shift ( $\Delta T$ ) Based on the CD-based Precipitation Model Predictions.

In order to provide perspective on the results of this study, we applied models previously developed by Odette et al [9, 16, 28, 31] to translate CD predictions of volume fraction ( $f_V$ ), number density ( $N$ ) and mean radius ( $r$ ) to yield stress increases ( $\Delta\sigma_y$ ) and to the associated ductile-to-brittle transition temperature shift ( $\Delta T$ ) with irradiation (see SI Sec. I for details). Note we do not claim that these examples represent actual quantitative predictions of anticipated embrittlement behavior. Figure 12 shows the predicted time and fluence dependence of  $f_V$  and  $\Delta T$ , respectively, for three different Ni levels (0.6at.%, 1.0% and 1.6%) with 1.00at.%Mn-0.40%Si (a medium solute concentration of Mn and a typical one for Si) at 290°C and a flux of  $3.6 \times 10^{14} \text{ m}^{-2} \text{ s}^{-1}$ , pertinent to RPV service. Figure 12a shows that the MNSPs are still in the rapid growth stage from 40 to 80 years. At an extended life fluence of  $10^{24} \text{ n} \cdot \text{m}^{-2}$  typical RPV steels with 1.0at.%Ni are predicted to contain  $f_V \approx 0.2\%$  MNSP that is capable of producing  $\Delta T \approx 80^\circ\text{C}$ . High 1.6%Ni steels contain  $f_V \approx 0.9\%$  MNSP at  $10^{24} \text{ n} \cdot \text{m}^{-2}$ , with corresponding  $\Delta T$  of  $250^\circ\text{C}$ . A map of the CD predictions for a wider range of compositions can be found in SI Sec. I.

## 8. Conclusions

A cluster dynamics model has been developed to study the evolution of Mn-Ni-Si precipitates (MNSPs) in low-Cu RPV steels, which lead to irradiation embrittlement. The model draws upon available thermodynamic and kinetic data, and includes a semi-empirical model for radiation-enhanced diffusion, including treatment of flux effects. The model also includes heterogeneous nucleation on damage created in displacement cascades. The interfacial energies

for MNSPs and heterogeneous nucleation rates and nucleated cluster sizes were determined by fitting to a large body of high quality experimental APT data. The model, which was calibrated to 10 alloys (with 33 different APT tip compositions) for a range of irradiation conditions, can semi-quantitatively predict for alloys with very high flux (ATR-1), where MNSPs are either underpredicted, or do not form, in contrast to experimental observations. In part this is due to the fact that the model underpredicts MNSP formation in the alloys studied here with medium Ni contents around 0.8 wt%, and comparison to a wider body of data not considered in this work supports that this is a general trend. We discuss various possible unmodeled physics explanations for these underpredictions that will be addressed in future research.

The principle conclusions derived from this study include:

1. A CD model has been developed to treat MNSP evolution in irradiated low Cu steels that predicts the slow precipitation of G/T3 and  $\Gamma_2$ /T6 phases at around 290°C, that can reach high mole fractions at high fluence.
2. The CD model is generally in qualitative, or semi quantitative agreement with experimental APT observations on the composition dependence of MNSP  $N$ ,  $r$  and  $f$ .
3. A heterogeneous mechanism for nucleating MNSPs is critical to their formation, except at the high Ni contents of >1.5at.%Ni, where homogeneous nucleation dominates. Heterogeneous nucleation is not needed at sufficiently high Ni due to a larger free energy difference driving precipitation.
4. The alloy Ni content is the dominant compositional factor in forming MNSPs, while Mn and Si play lesser roles. The dominant role of Ni is due to the fact the G and  $\Gamma_2$  phases respectively contain 1 and 0.8 (Mn + Si) atoms for every Ni atom, respectively.
5. The absolute threshold for MNSPs formation appears to be  $\approx 0.5$ at.%Ni.

6. The model suggests that MNSPs in low Cu alloys in RPVs are in a nucleation and growth stage in present reactors, with significantly more hardening and associated temperature shifts expected during life-extension.
7. As an illustrative example, at an extended life fluence of  $10^{24}\text{n}\cdot\text{m}^{-2}$  typical RPV steels with 1.0at.%Ni and 1.6at.%Ni are predicted to contain  $f_V \approx 0.2\%$  and 0.9% MNSPs that are capable of producing  $\Delta T \approx 80^\circ\text{C}$  and  $250^\circ\text{C}$ , respectively.
8. The mole fractions of MNSPs under very high flux at very high fluence (ATR-1) observed from experiments are even higher than the value predicted by CALPHAD model at equilibrium without considering Gibbs-Thomson effect. Thus even with cascade enhanced nucleation, the CD model under-predicted the mole fraction of MNSPs in this case. This suggests that unmodeled other physics, like influence of small amounts of Cu, or segregation resulting in precipitation on small dislocation loops, may play a significant role under this extreme condition.
9. The MNSP mole fraction of medium Ni steels (BR2-TU, BR2-G1 LG and Ginna) are under predicted compared to experiment. The differences may again be due to either thermodynamic model inaccuracies, or unmodeled physics.
10. We note that a major limitation of the model for real RPVs is that Cu is not treated in the CD model, but it is well established that even small concentrations, below the amounts needed to produce well-formed Cu enriched precipitates, catalyze the formation of MNSPs.

Although Cu is not included in the present model, it will serve as a foundation for future modeling of Cu-Mn-Ni-Si precipitation in Cu bearing RPV steels. Further, many simplifications and approximations in the current CD will be improved and additional physics included,

especially treating nucleation in a more rigorous fashion. Notably, the CD model, and its improved progeny, will be compared to and informed by a growing RPV steel database, especially the results of the UCSB ATR-2 high fluence irradiation program. Finally, these detailed physics-based models will inform reduced order model, but still physically based, correlation equations fit to the actual surveillance and test reactor databases. Ultimately, the more detailed models themselves might be fit these databases to provide an even more detailed physical basis for embrittlement prediction interpolation and extrapolation.

## **Acknowledgements**

This work has been primarily supported by the US Department of Energy Office of Nuclear Energy's Light Water Reactor Sustainability Program, Materials Aging and Degradation Pathway. Partial support for Huibin Ke was provided by the DOE Office of Nuclear Energy's Integrated Research Project (IRP) under contract DE-NE0000639. A portion of this research, both the ATR irradiation and FIB/APT at the Center for Advanced Energy Studies - Microscopy and Characterization Suite (CAES-MaCS), was supported by the Advanced Test Reactor National Scientific User Facility through the U.S. Department of Energy, Office of Nuclear Energy under DOE Idaho Operations Office Contract DE-AC07-05ID14517. We also would like to thank Dr. Takuya Yamamoto at the University of California-Santa Barbara who helped with the hardening model in this work. Special thanks go to Collin Knight at the Idaho National Laboratory for assisting in the complex steps needed to gain access to the irradiated ATR specimens. The much earlier piggyback BR2 irradiations were sponsored by Jean Claude Van Duysen of Electricite de France and carried out under the supervision of Lorenzo Malerbra at SCK Belgium. We also thank Peter Hosemann at UC Berkeley for access to their FIB to prepare APT samples from the BR2 (TU, G1 and G2) conditions. The MRL Shared Experimental

Facilities were used for performing APT on the BR2 samples and are supported by the MRSEC Program of the NSF under Award No. DMR 1121053 as a member of the NSF-funded Materials Research Facilities Network ([www.mrfn.org](http://www.mrfn.org)). The bulk of this research was supported by the DOE Office of Nuclear Energy's Nuclear Energy University Program, as part of the LRW Sustainability Task.

## Reference

- [1] Country Statistics - United States of America. IAEA - International Atomic Energy Agency, 2015.
- [2] S. Chu, A. Majumdar. Opportunities and challenges for a sustainable energy future, *Nature* 488 (2012) 294-303.
- [3] Technology Roadmap - Nuclear Energy. Nuclear Energy Agency, 2015.
- [4] J.T. Busby, P.G. Oberson, C.E. Carpenter, M. Srinivasan. Expanded Materials Degradation Assessment. Executive Summary of EMDA Process and Results, vol. 1: Office of Nuclear Regulatory Research, 2013.
- [5] J.T. Busby, P.G. Oberson, C.E. Carpenter, M. Srinivasan. Expanded Materials Degradation Assessment. Aging of Reactor Pressure Vessels, vol. 3: Office of Nuclear Regulatory Research, 2013.
- [6] G.R. Odette, G.E. Lucas. Embrittlement of nuclear reactor pressure vessels, *The Journal of The Minerals, Metals & Materials Society (TMS)* 53 (2001) 18-22.
- [7] G.R. Odette, R.K. Nanstad. Predictive reactor pressure vessel steel irradiation embrittlement models: issues and opportunities, *Journal of the Minerals, Metals and Materials Society* 61 (2009) 17-23.
- [8] G.R. Odette. Radiation Induced Microstructural Evolution In Reactor Pressure Vessel Steels. In: Robertson IM, Rehn LE, Zinkle SJ, Phythian WJ, (Eds.). *Materials Research Society Symposium Proceedings*, vol. 373. Warrendale: Materials Research Society, 1995. p.137-148.
- [9] G.R. Odette, G.E. Lucas. Recent progress in understanding reactor pressure vessel steel embrittlement, *Radiation Effects and Defects in Solids* 144 (1998) 189-231.
- [10] C.L. Liu, G.R. Odette, B.D. Wirth, G.E. Lucas. A lattice Monte Carlo simulation of nanophase compositions and structures in irradiated pressure vessel Fe-Cu-Ni-Mn-Si steels, *Materials Science and Engineering A* 238 (1997) 202-209.
- [11] G.R. Odette, B.D. Wirth. A computational microscopy study of nanostructural evolution in irradiated pressure vessel steels, *Journal of Nuclear Materials* 251 (1997) 157-171.
- [12] G. Odette. On the dominant mechanism of irradiation embrittlement of reactor pressure vessel steels, *Scripta metallurgica* 17 (1983) 1183-1188.
- [13] J.M. Hyde, G. Sha, E.A. Marquis, A. Morley, K.B. Wilford, T.J. Williams. A comparison of the structure of solute clusters formed during thermal ageing and irradiation, *Ultramicroscopy* 111 (2011) 664-671.

[14] P.D. Styman, J.M. Hyde, K. Wilford, a. Morley, G.D.W. Smith. Precipitation in long term thermally aged high copper, high nickel model RPV steel welds, *Progress in Nuclear Energy* 57 (2012) 86-92.

[15] M.K. Miller, K.F. Russell. Embrittlement of RPV steels: An atom probe tomography perspective, *Journal of Nuclear Materials* 371 (2007) 145-160.

[16] P.B. Wells, T. Yamamoto, B. Miller, T. Milot, J. Cole, Y. Wu, G.R. Odette. Evolution of manganese-nickel-silicon-dominated phases in highly irradiated reactor pressure vessel steels, *Acta Materialia* 80 (2014) 205-219.

[17] G.R. Odette, T. Yamamoto, D. Klingensmith. The Effect of Dose Rate on Irradiation Hardening of RPV Steels: A Comprehensive Single Variable Database and Model Based Analysis. Washington, D.C.: U.S. Nuclear Regulatory Commission, 2003.

[18] G.R. Odette, T. Yamamoto, B.D. Wirth. Late blooming phases and dose rate effects in RPV steels: integrated experiments and models. In: Ghoniem NM, (Ed.). *Second International Conference on Multiscale Materials Modeling*. Los Angeles, 2004. p.355.

[19] M.K. Miller, M.A. Sokolov, R.K. Nanstad, K.F. Russell. APT characterization of high nickel RPV steels, *Journal of Nuclear Materials* 351 (2006) 187-196.

[20] M.K. Miller, A.A. Chernobaeva, Y.I. Shtrombakh, K.F. Russell, R.K. Nanstad, D.Y. Erak, O.O. Zabusov. Evolution of the nanostructure of VVER-1000 RPV materials under neutron irradiation and post irradiation annealing, *Journal of Nuclear Materials* 385 (2009) 615-622.

[21] M.K. Miller, K.A. Powers, R.K. Nanstad, P. Efsing. Atom probe tomography characterizations of high nickel, low copper surveillance RPV welds irradiated to high fluences, *Journal of Nuclear Materials* 437 (2013) 107-115.

[22] P.D. Edmondson, M.K. Miller, K.A. Powers, R.K. Nanstad. Atom probe tomography characterization of neutron irradiated surveillance samples from the R. E. Ginna reactor pressure vessel, *Journal of Nuclear Materials* 470 (2016) 147-154.

[23] NRC. *Radiation Embrittlement of Reactor Vessel Materials*. Rugulatory Guide 1.99 Revision 2. Washington, D. C.: Office of Nuclear Regulatory Research, US Nuclear Regulatory Commission, 1998.

[24] J.W.P. Schmelzer. A new approach to nucleation theory and its application to phase formation processes in glass-forming melts, *Physics and Chemistry of Glasses* 45 (2004) 116-120.

[25] J.W.P. Schmelzer, A.S. Abyzov, J. Moller. Nucleation versus spinodal decomposition in phase formation processes in multicomponent solutions, *Journal of Chemical Physics* 121 (2004) 6900-6917.

[26] J.W.P. Schmelzer, A.R. Gokhman, V.M. Fokin. Dynamics of first-order phase transitions in multicomponent systems: a new theoretical approach, *Journal of Colloid and Interface Science* 272 (2004) 109-133.

[27] V. Slezov. *Kinetics of First-Order Phase Transitions*, (2009) 7-38.

[28] E.D. Eason, G.R. Odette, R.K. Nanstad, T. Yamamoto. A Physically Based Correlation of Irradiation-Induced Transition Temperature Shifts for RPV Steels. 2007.

[29] C. Domain, C.S. Becquart. Ab initio calculations of defects in Fe and dilute Fe-Cu alloys, *Physical Review B* 65 (2001).

[30] G.R. Odette, T. Yamamoto, D. Klingensmith. On the effect of dose rate on irradiation hardening of RPV steels, *Philosophical Magazine* 85 (2005) 779-797.

[31] E.D. Eason, G.R. Odette, R.K. Nanstad, T. Yamamoto. A physically-based correlation of irradiation-induced transition temperature shifts for RPV steels, *Journal of Nuclear Materials* 433 (2013) 240-254.

[32] D.W. James, G.M. Leak. Self-diffusion and Diffusion of Cobalt in Alpha and Delta-iron, *Philosophical Magazine* 14 (1966) 701.

[33] G. Hettich, H. Mehrer, K. Maier. Self-diffusion in ferromagnetic  $\alpha$ -iron, *Scripta Materialia* 11 (1977) 795-802.

[34] Y. Iijima, K. Kimura, K. Hirano. SELF-DIFFUSION AND ISOTOPE EFFECT IN  $\alpha$ -IRON, *Acta Metallurgica* 36 (1988) 2811-2820.

[35] F.S. Buffington, K. Hirano, M. Cohen. Self diffusion in Iron, *Acta Materialia* 9 (1961) 434-439.

[36] J. Bernabdini, P. Gas, E.D. Hondbos, M.P. Seah. The role of solute segregation in grain boundary diffusion, *Proceedings of the Royal Society of London Series A* 379 (1982) 159-178.

[37] D. Graham. Mass Dependence of Self-Diffusion in Iron, *Journal of Applied Physics* 40 (1969) 2386.

[38] M. Lubbehusen, H. Mehrer. Self-diffusion in  $\alpha$ -Iron: The influence of dislocations and the effect of the magnetic phase transition, *Acta Metall Mater* 38 (1990) 283-292.

[39] K. Nohara, K. Hirano. Diffusion of Mn(54) in iron and iron-manganese alloys. International Conference on Science and Technology of Iron and Steels, vol. 7: The Iron and Steel Institute of Japan, 1971. p.1267.

[40] K. Hirano, M. Cohen, B.L. Averbach. Diffusion of nickel into iron, *Acta Materialia* 9 (1961) 440-445.

[41] M. Bachhav, G. Robert Odette, E.A. Marquis.  $\alpha'$  precipitation in neutron-irradiated Fe - Cr alloys, *Scripta Materialia* 74 (2014) 48-51.

[42] J.O. Andersson, T. Helander, L. Höglund, P. Shi, B. Sundman. Thermo-Calc & DICTRA, computational tools for materials science, *Calphad: Computer Coupling of Phase Diagrams and Thermochemistry* 26 (2002) 273-312.

[43] Thermo-Calc Software TCAL2 / Aluminum database version 2, (Assessed 20 Sep 2014).

[44] W. Xiong, H. Ke, R. Krishnamurthy, P. Wells, L. Barnard, G.R. Odette, D. Morgan. Thermodynamic models of low-temperature Mn–Ni–Si precipitation in reactor pressure vessel steels, *MRS Communications* (2014) 101-105.

[45] K.P. Gupta. The Mn–Ni–Si (Manganese–Nickel–Silicon) System, *Journal of Phase Equilibria & Diffusion* 27 (2006) 529-534.

[46] B. Hu, H. Xu, S. Liu, Y. Du, C. He, C. Sha, D. Zhao, Y. Peng. Experimental investigation and thermodynamic modeling of the Mn–Ni–Si system, *Calphad* 35 (2011) 346-354.

[47] R. Ngayam-Happy, C.S. Becquart, C. Domain. First principle-based AKMC modelling of the formation and medium-term evolution of point defect and solute-rich clusters in a neutron irradiated complex Fe–CuMnNiSiP alloy representative of reactor pressure vessel steels, *Journal of Nuclear Materials* 440 (2013) 143-152.

[48] R. Ngayam-Happy, C.S. Becquart, C. Domain, L. Malerba. Formation and evolution of MnNi clusters in neutron irradiated dilute Fe alloys modelled by a first principle-based AKMC method, *Journal of Nuclear Materials* 426 (2012) 198-207.

[49] G. Bonny, D. Terentyev, a. Bakaev, E.E. Zhurkin, M. Hou, D. Van Neck, L. Malerba. On the thermal stability of late blooming phases in reactor pressure vessel steels: An atomistic study, *Journal of Nuclear Materials* 442 (2013) 282-291.

- [50] R.J. Borg. Diffusion in  $\alpha$ -Fe-Si Alloys, *Journal of Applied Physics* 41 (1970) 5193.
- [51] F. Christien, A. Barbu. Modelling of copper precipitation in iron during thermal aging and irradiation, *Journal of Nuclear Materials* 324 (2004) 90-96.
- [52] G.R. Odette. Private Communication (2015).
- [53] B. Gault, M.P. Moody, J.M. Caimey, S.P. Ringer. *Atom probe microscopy*, Springer New York Heidelberg Dordrecht London, New York, 2012.

## List of Figures

Figure 1 Schematic plot of homogeneous and heterogeneous nucleation mechanisms applied used in the cluster dynamics model. ....	37
Figure 2 Thermodynamic equilibrium CALPHAD predictions. a) precipitate compositions compared to APT data; b) precipitate solute mole fractions; c) phase selection fractions. ....	38
Figure 3 Evolution of precipitates in the high Ni CM6 and the medium Ni LG as a function of fluence compared to the APT data for the various irradiation conditions. The lines represent simulated data for single APT tip composition, while for multiple APT tips and associated compositions are shown as the shaded bands. ....	39
Figure 4 Evolution of precipitates as a function of fluence compared to the APT data for the various irradiation conditions for Ringhals and Ginna power reactors. ....	40
Figure 5 A comparison between the Ringhals N alloy irradiated at low flux ( $1.49 \times 10^{15} \text{m}^{-2}\text{s}^{-1}$ ) and the CM6 alloy irradiated at high flux ( $2.3 \times 10^{18} \text{m}^{-2}\text{s}^{-1}$ ). The CM6 data at lower flux are shifted to higher fluence due to the dose rate effect. The CM6 are adjusted to a common ATR-1 reference flux, as indicated by the arrows, using the simple <i>p</i> -scaling effective fluence model. In this case the effect of flux is somewhat under predicted for the common value of <i>p</i> = 0.2 ....	41
Figure 6 Comparison of the CD number density, mean radius and mole fraction and the APT data. ....	42
Figure 7 The ratio of number of precipitates created by heterogeneous to homogeneous nucleation at different fluences. ....	43
Figure 8 The effects of Mn and Ni on the evolution of precipitate at $1 \times 10^{16} \text{m}^{-2}\text{s}^{-1}$ at 290°C for: a) 0.35at.% and b) 0.45at%. ....	44

Figure 9 The effect of temperature on the evolution of MNS precipitates for: a) Fe-1.45at.%Mn-1.65%Ni-0.45%Si; and, b) Fe-1.00at.%Mn-0.70%Ni-0.35%Si .....	45
Figure 10 The square root of mole fraction ( $\sqrt{f}$ ) as a function of Ni composition for various Mn and Si contents at different fluences .....	46
Figure 11 The effect of temperature on $\sqrt{f}$ for various alloy Ni contents with 1.4at.%Mn-0.6%Si and two fluences: a) absolute $\sqrt{f}$ ; and, b) normalized to 1 at 290°C.....	47
Figure 12 CD model predictions of the effect of Ni at 1.00at.%Mn-0.40%Si and a flux of $3.6 \times 10^{14} \text{ m}^{-2} \text{ s}^{-1}$ at 290°C: a) $\sqrt{f}$ ; and, b) $\Delta T$ with various.....	48

## **List of Tables**

Table 1 The alloy compositions and irradiation conditions in this study.....	16
Table 2 The crystal structures of Mn-Ni-Si phases in RPV steels at around 300°C .....	18
Table 3 The equilibrium solute product for the G-phase (T3) and $\Gamma_2$ -phase (T6) at different temperatures.....	19
Table 4 The thermal diffusion coefficients used in this study.....	19
Table 5 The model parameters used in calculating the radiation enhanced diffusion coefficient and other parameters used in cluster dynamics model. ....	20

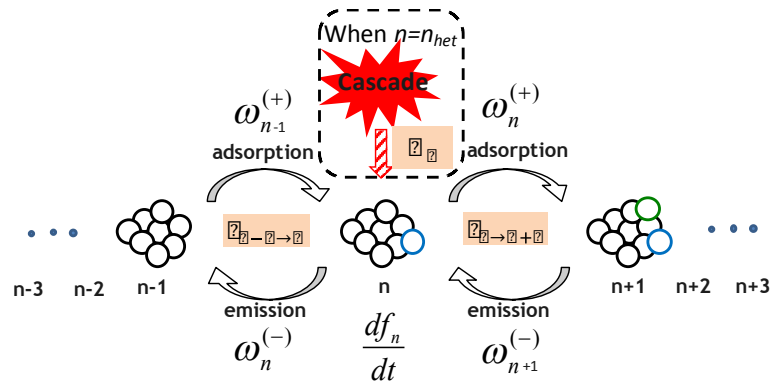


Figure 1 Schematic plot of homogeneous and heterogeneous nucleation mechanisms applied used in the cluster dynamics model.

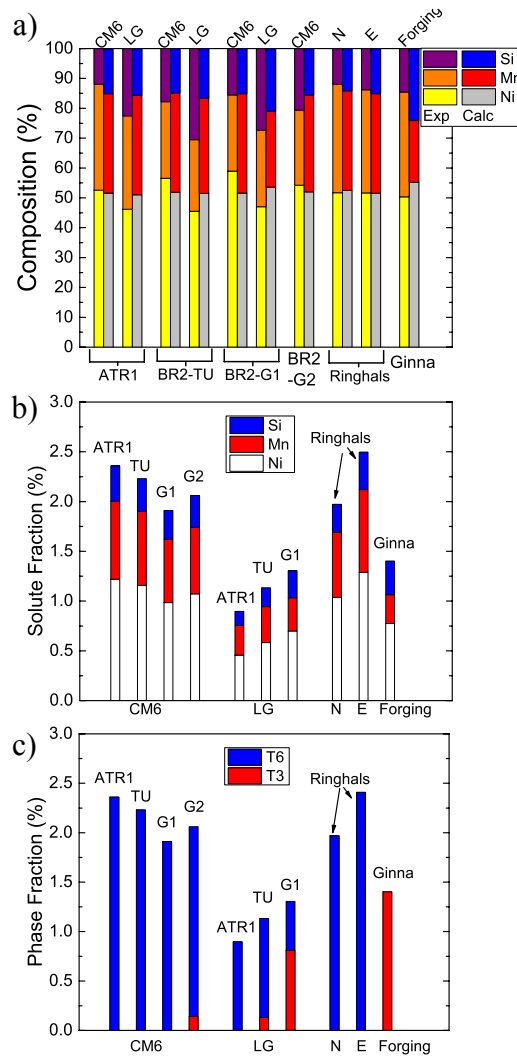


Figure 2 Thermodynamic equilibrium CALPHAD predictions.

a) precipitate compositions compared to APT data; b) precipitate solute mole fractions; c) phase selection fractions.

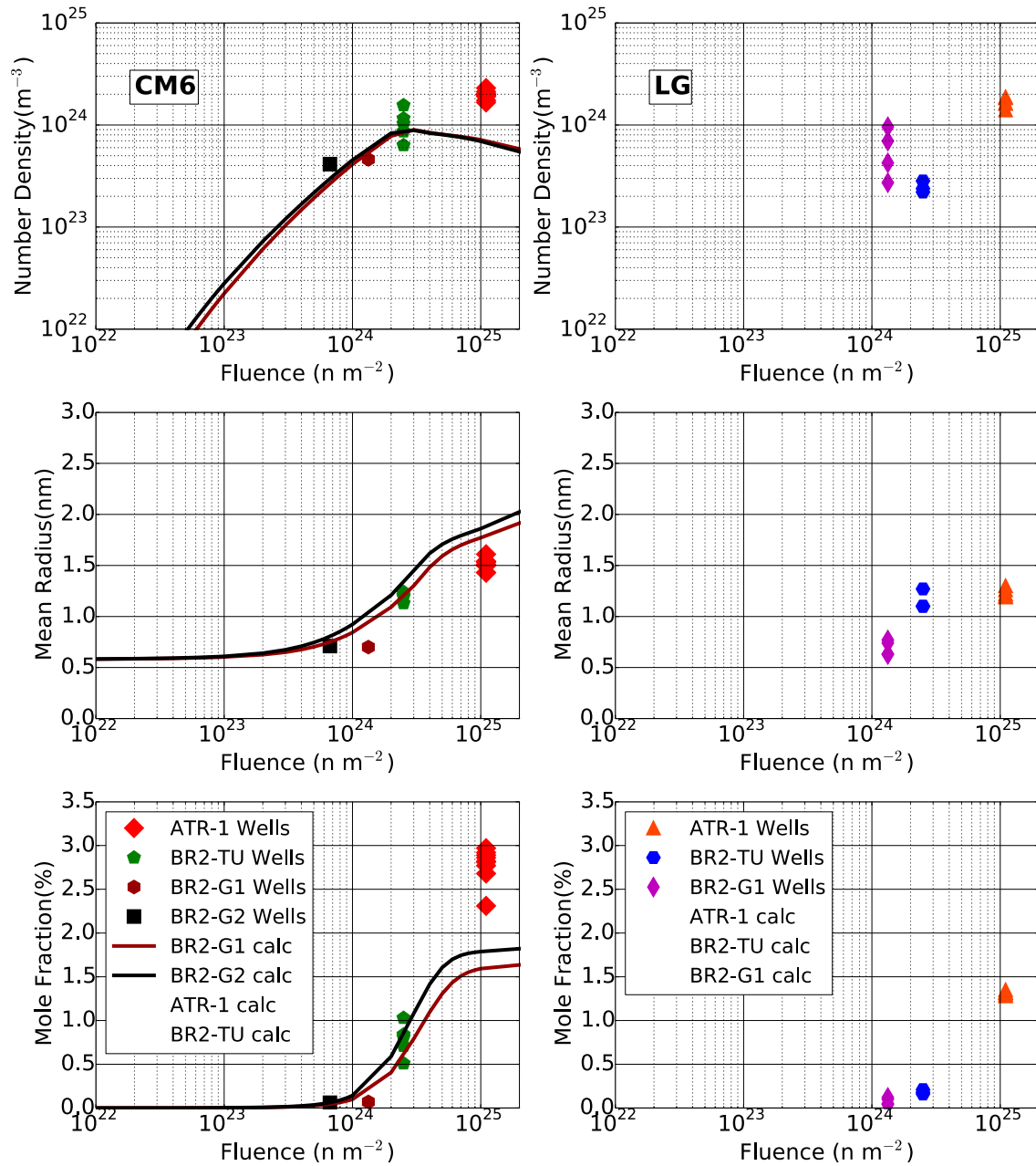


Figure 3 Evolution of precipitates in the high Ni CM6 and the medium Ni LG as a function of fluence compared to the APT data for the various irradiation conditions. The lines represent simulated data for single APT tip composition, while for multiple APT tips and associated compositions are shown as the shaded bands.

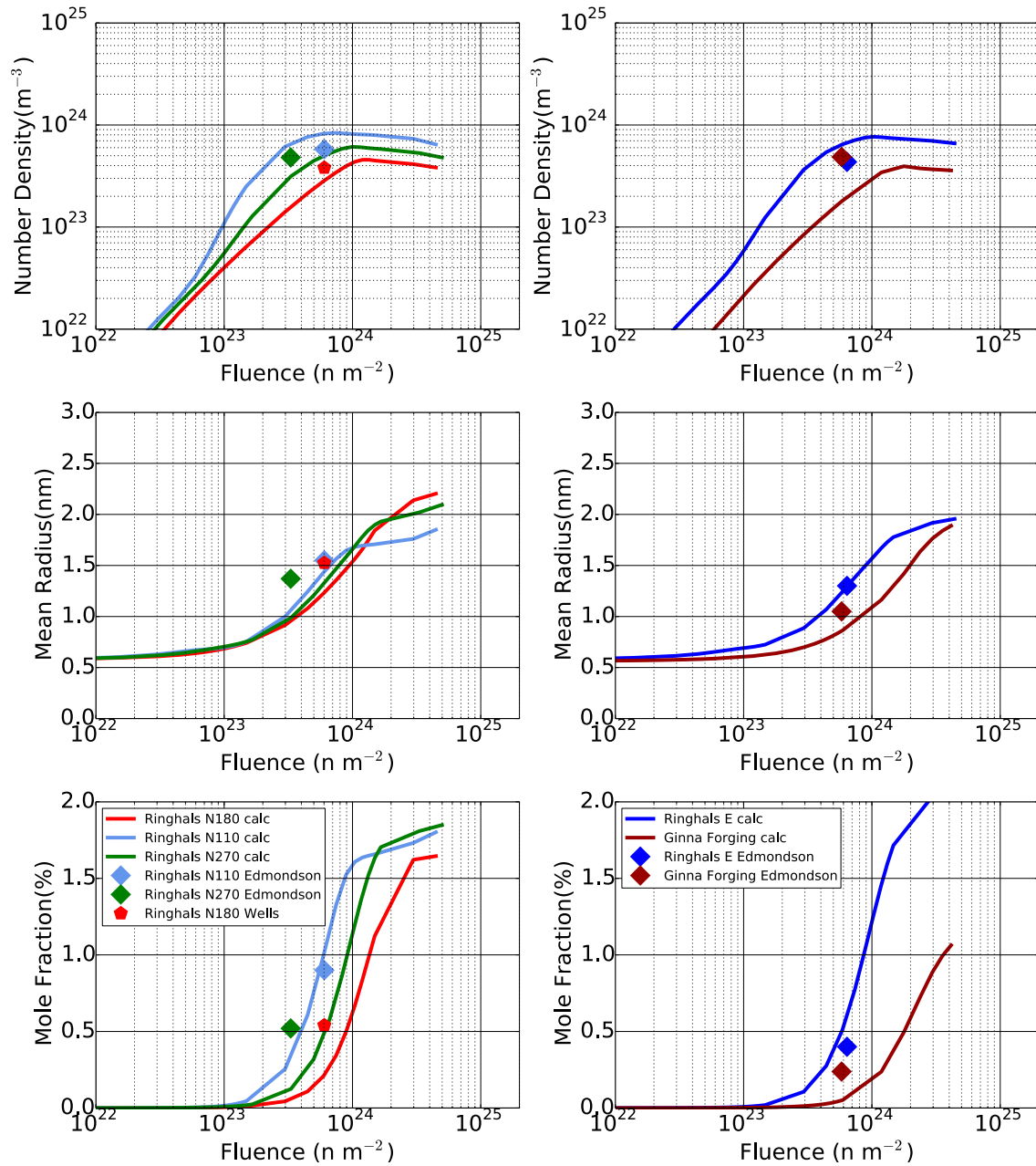


Figure 4 Evolution of precipitates as a function of fluence compared to the APT data for the various irradiation conditions for Ringhals and Ginna power reactors.

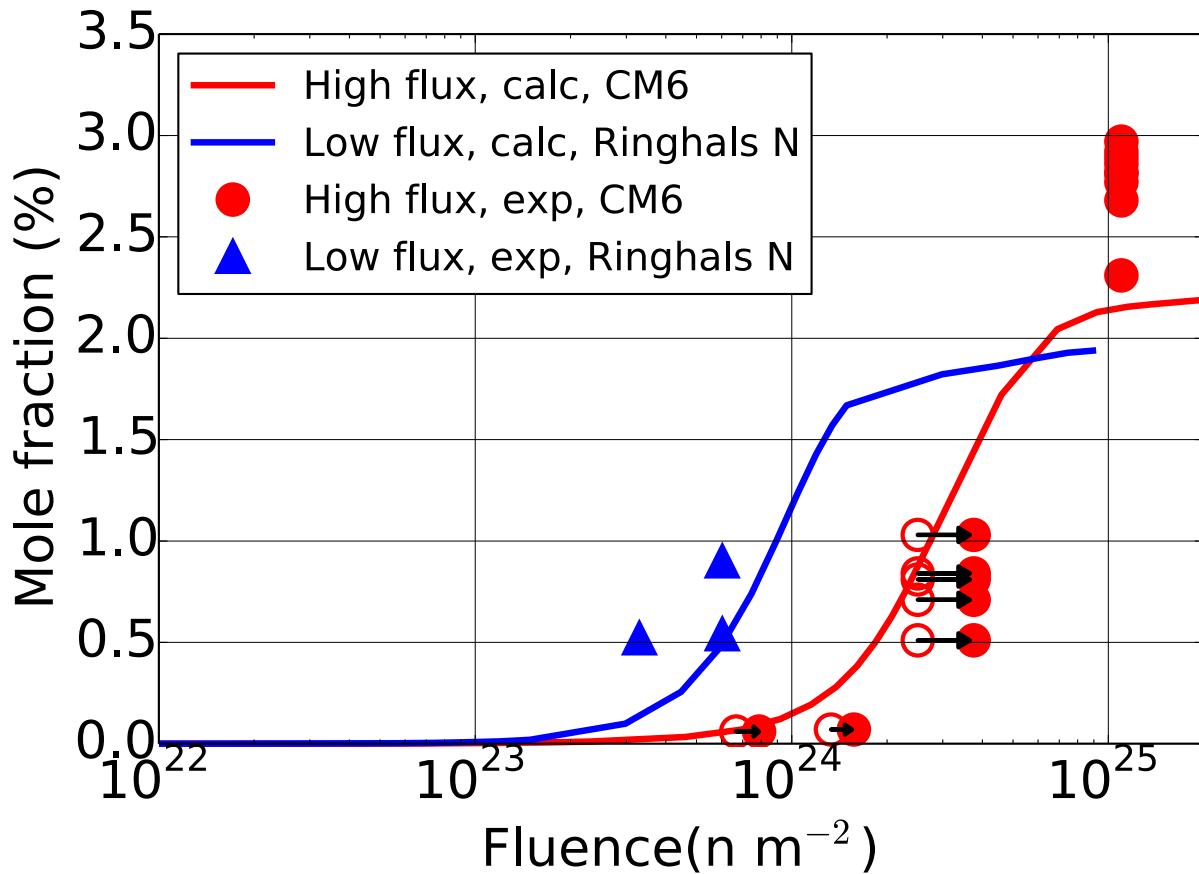


Figure 5 A comparison between the Ringhals N alloy irradiated at low flux ( $1.49 \times 10^{15} \text{ m}^{-2} \text{s}^{-1}$ ) and the CM6 alloy irradiated at high flux ( $2.3 \times 10^{18} \text{ m}^{-2} \text{s}^{-1}$ ). The CM6 data at lower flux are shifted to higher fluence due to the dose rate effect. The CM6 are adjusted to a common ATR-1 reference flux, as indicated by the arrows, using the simple  $p$ -scaling effective fluence model. In this case the effect of flux is somewhat under predicted for the common value of  $p = 0.2$

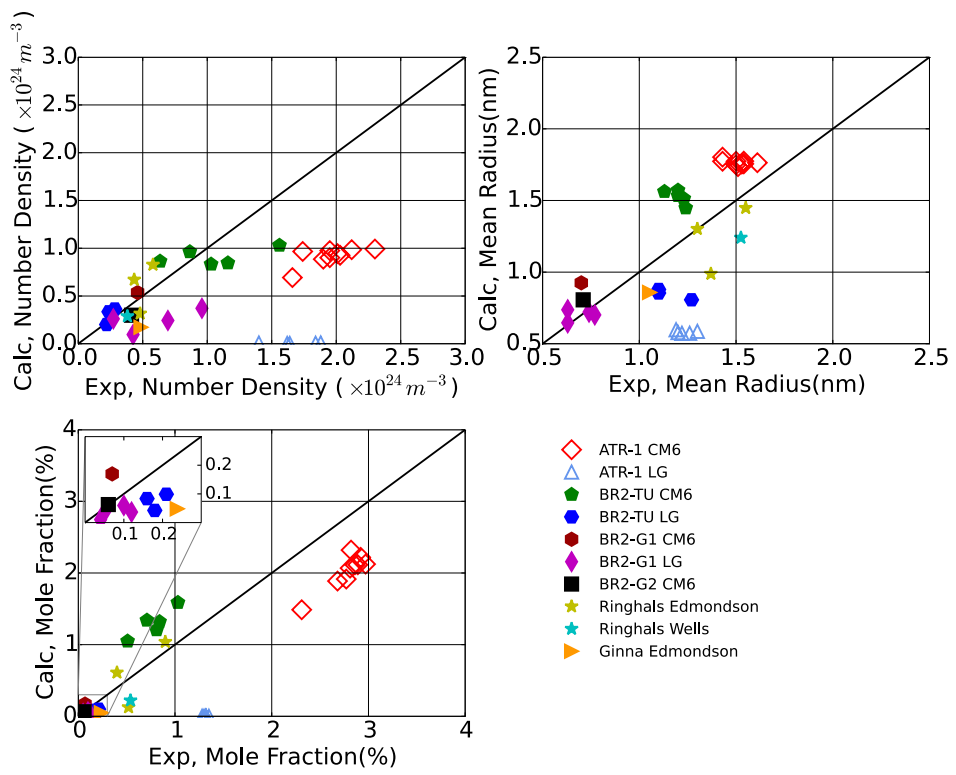


Figure 6 Comparison of the CD number density, mean radius and mole fraction and the APT data.

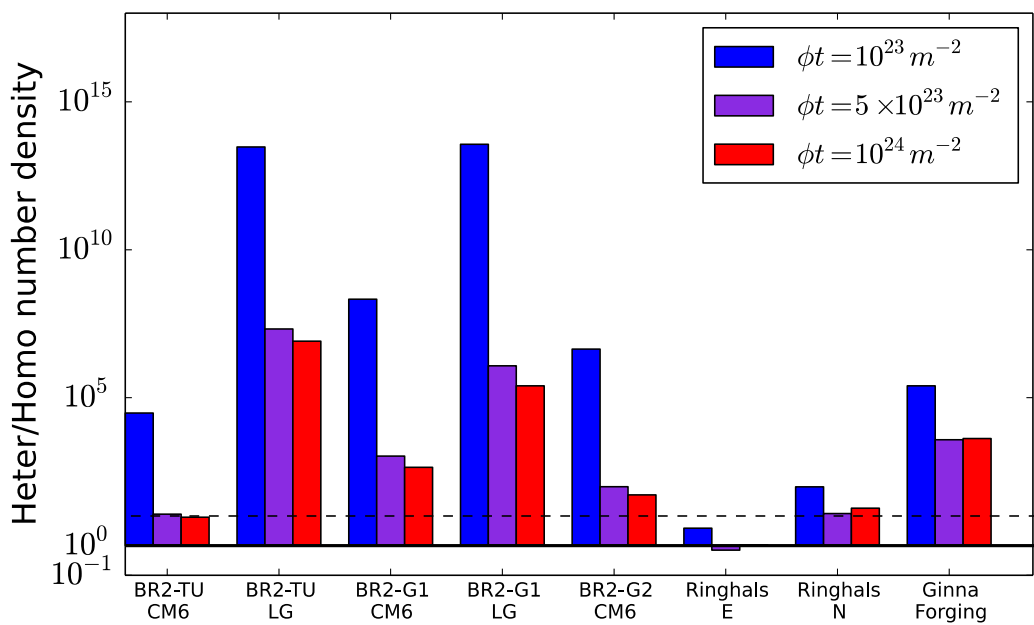


Figure 7 The ratio of number of precipitates created by heterogeneous to homogeneous nucleation at different fluences.

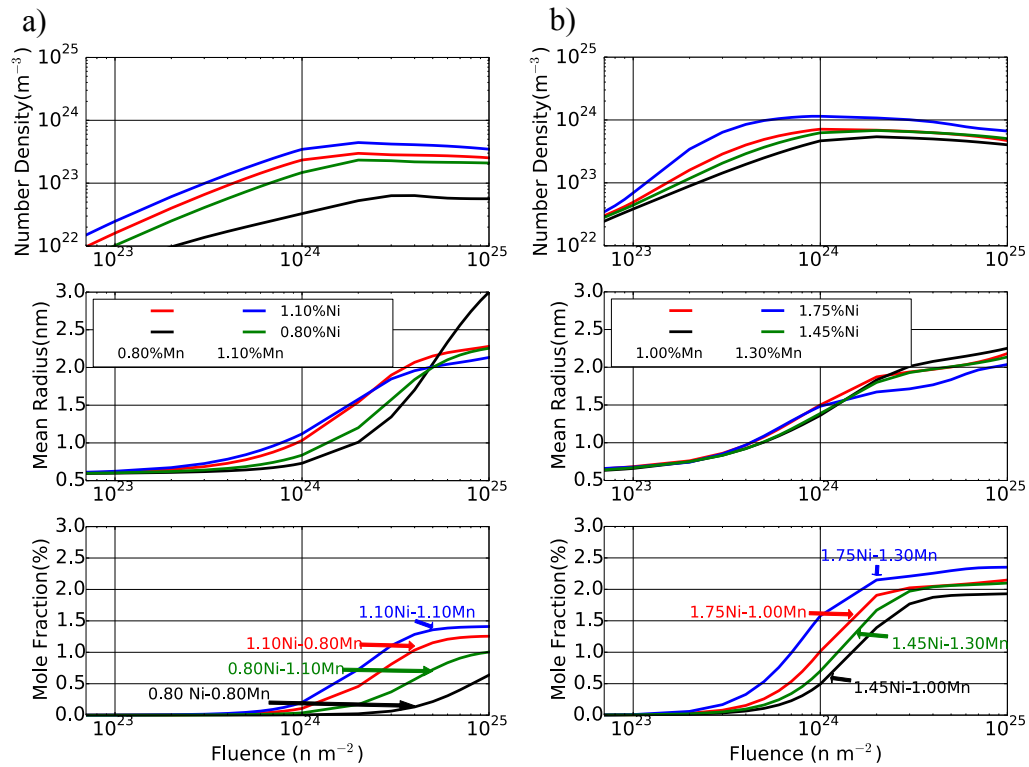


Figure 8 The effects of Mn and Ni on the evolution of precipitate at  $1 \times 10^{16} \text{ m}^{-2} \text{s}^{-1}$  at  $290^\circ\text{C}$  for: a) 0.35 at.-% and b) 0.45 at.-%.

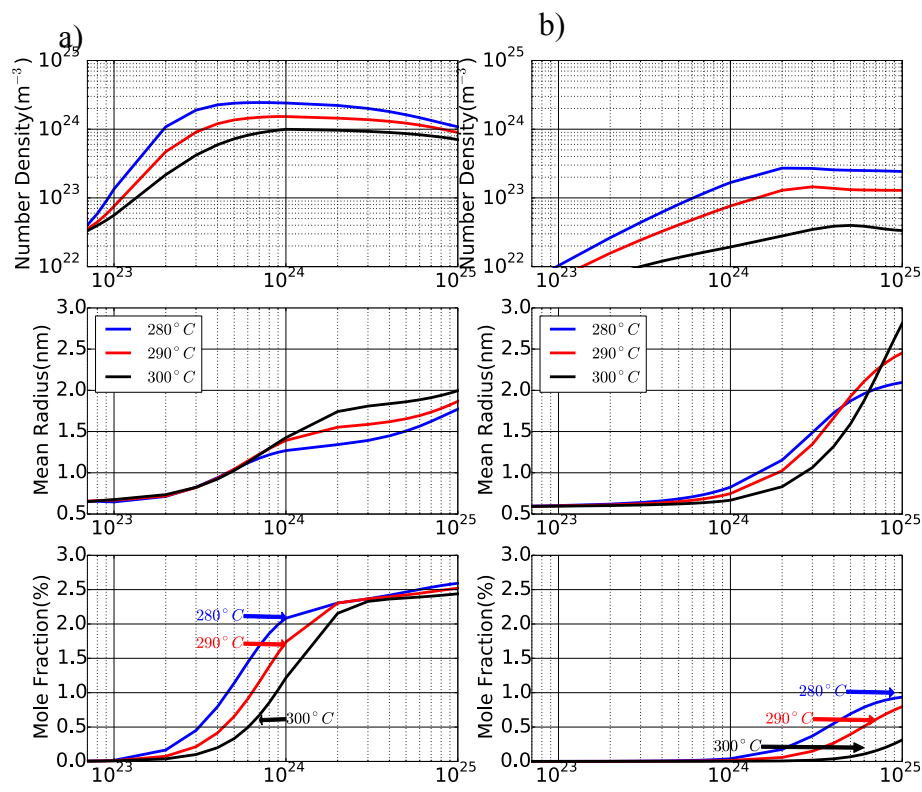


Figure 9 The effect of temperature on the evolution of MNS precipitates for: a) Fe-1.45at.%Mn-1.65%Ni-0.45%Si; and, b) Fe-1.00at.%Mn-0.70%Ni-0.35%Si.

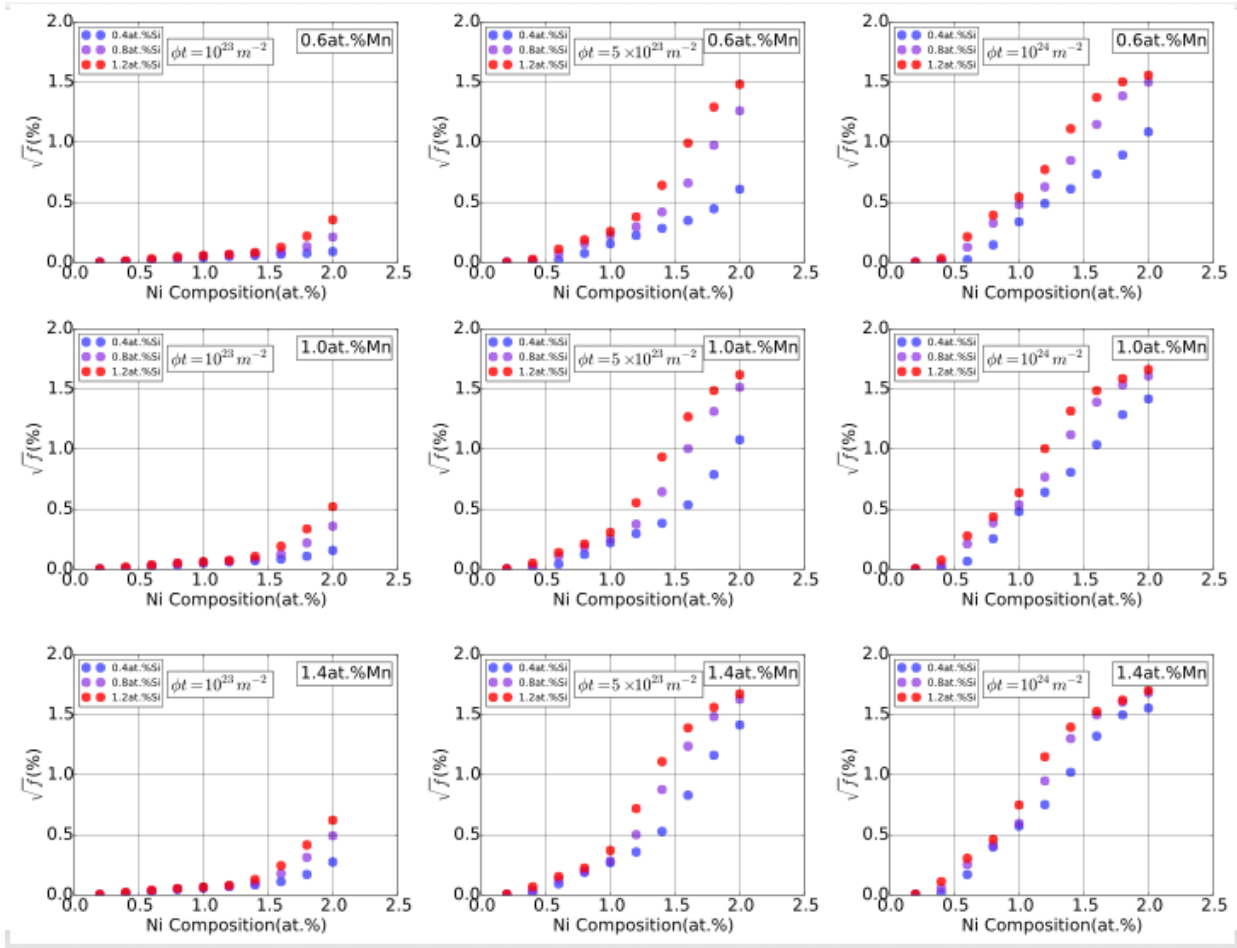


Figure 10 The square root of mole fraction ( $\sqrt{f}$ ) as a function of Ni composition for various Mn and Si contents at different fluences.

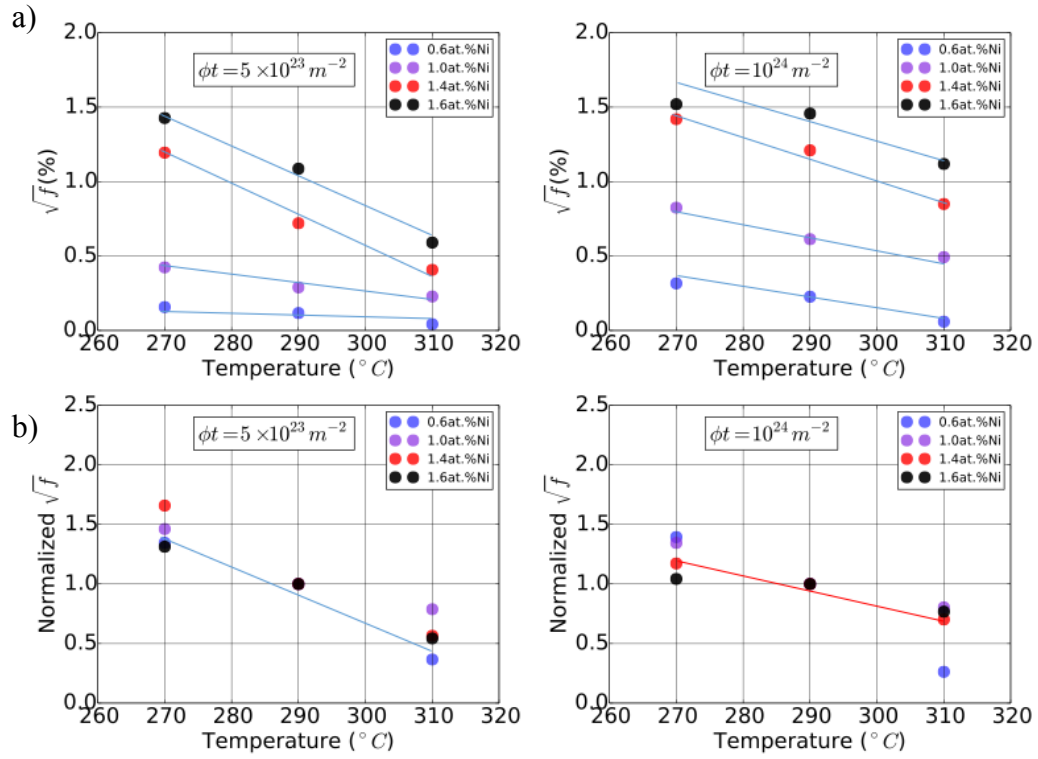


Figure 11 The effect of temperature on  $\sqrt{f}$  for various alloy Ni contents with 1.4at.%Mn-0.6%Si and two fluences: a) absolute  $\sqrt{f}$ ; and, b) normalized to 1 at 290°C.

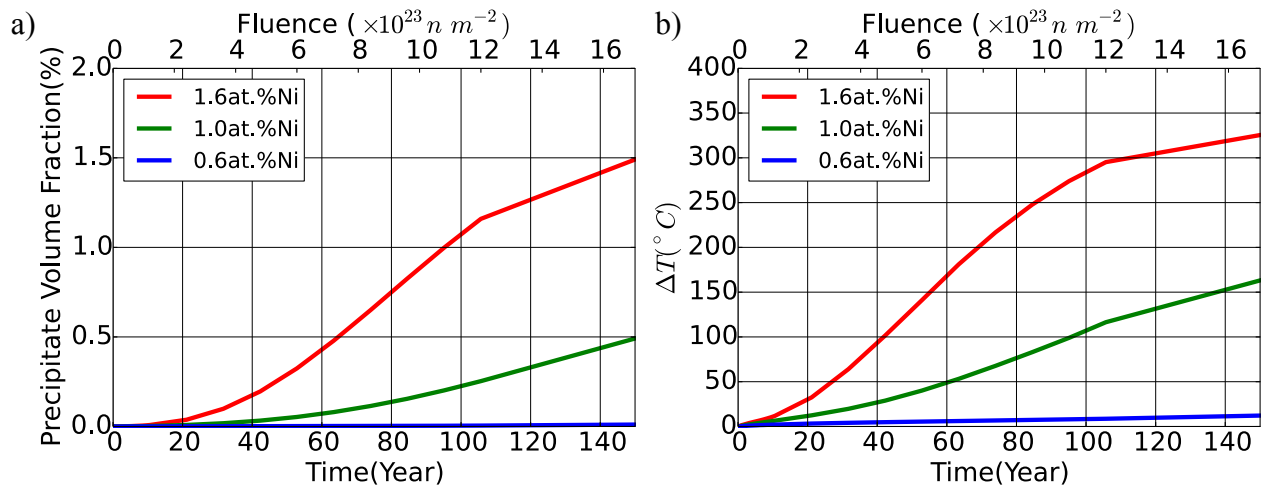


Figure 12 CD model predictions of the effect of Ni at 1.00at.%Mn-0.40%Si and a flux of  $3.6 \times 10^{14} m^{-2}s^{-1}$  at  $290^{\circ}C$ : a)  $\sqrt{f}$ ; and, b)  $\Delta T$  with various.